The BEACH Domain-Containing Protein SPIRRIG Modulates Actin-Dependent Root Hair Development in Coordination with the WAVE/SCAR and ARP2/3 Complexes

Sabrina Chin[a] , Taegun Kwon[a], Bibi Rafeiza Khan[a, 2], J. Alan Sparks[a], Eileen L. Mallery[b], Daniel B. Szymanski[b,c] and Elison B. Blancaflor[a, 1]

[a] Noble Research Institute LLC, 2510 Sam Noble Parkway, Ardmore, Oklahoma 73401,

[b] Department of Botany and Plant Pathology, [c] Dept. of Biological Sciences, Purdue University, West Lafayette, Indiana 47907

ORCID IDs: 0000-0003-3897-3812 (S.C.); 0000-0002-0205-8535 (T.K.); 0000-0002-7661-0142 (B.R.K.); 0000-0002-4492-9810 (J.A.S.); 0000-0002-0363-5920 (E.L.M.), 0000-0001-8255-424X (D.B.S.); 0000-0001-6115-9670 (E.B.B.)

[1] Address correspondence to eblancaflor@noble.org

[2]Current address: Department of Biology, University of Guyana, Turkeyen Campus, 41 Georgetown, Guyana

Short Title: Actin-mediated root hair development

The author responsible for distribution of materials integral to the findings presented in this article in accordance with the policy described in the Instructions for Authors are: Daniel B. Szymanski (szymandb@purdue.edu) and Elison B. Blancaflor (eblancaflor@noble.org).

Abstract

Root hairs are single cell protrusions that enable roots to optimize nutrient and water acquisition. They attain their tubular shapes by confining growth to the cell apex, a process called tip growth. The actin cytoskeleton and endomembrane system are essential for tip growth; however, little is known about how these cellular components coordinate their activities during this process. Here, we show that SPIRRIG (SPI), a BEACH domain-containing protein involved in membrane trafficking, and BRK1 and SCAR2, subunits of the WAVE/SCAR (W/SCR) and actin related protein (ARP)2/3 activation complexes, display polarized localizations to root hairs at distinct developmental stages. SPI accumulates at the root hair apex via post-Golgi vesicles and positively regulates tip growth by maintaining tip-focused vesicle secretion and filamentous-actin integrity. BRK1 and SCAR2 on the other hand, mark the root hair initiation domain to specify the position of root hair emergence. Live cell microscopy revealed that BRK1 depletion coincided with SPI accumulation as root hairs transitioned from initiation to tip growth. Furthermore, double mutant studies showed that *SPI* genetically interacts with *BRK1* and *ARP2/3*. Taken together, our work uncovers a role for SPI in facilitating actin-dependent root hair development through pathways that intersect with the W/SCR and ARP2/3 complexes.

INTRODUCTION

Root hairs are single cell tubular projections that emerge from root epidermal cells. They increase the effective surface area of the root system by extending laterally into soil pores, thus enabling the increased access to nutrients and water (Carminati et al., 2017, Ruiz et al., 2020). Root hairs have been studied extensively by plant biologists for decades because they serve as excellent models to unravel mechanisms by which cell size and shape in plants is regulated (Grierson et al., 2014). To attain their cylindrical shapes, root hairs undergo tip growth, a process in which expansion of the cell is confined to its apical domain. Tip growth involves a balance between the directed delivery of post-Golgi vesicles carrying protein complexes and cell wall building blocks to the cell apex, and localized cell wall loosening and recycling of excess membranes. Besides root hairs, tip growth is exhibited by other cell types such as pollen tubes, fungal hyphae, and rhizoids of mosses, liverworts and algae (Bascom et al., 2018a).

Root epidermal cells called trichoblasts are the cell types that form root hairs. Work in *Arabidopsis thaliana* has shown that trichoblasts are specified to become root hair-forming cells early during root development through the patterned assembly of protein complexes of transcriptional activators and repressors in different cell files (Schiefelbein et al., 2014, Shibata et al., 2018). Upon establishing their identity, trichoblasts undergo two developmental stages that lead to root hair outgrowth. The first stage is the establishment of a root hair initiation domain (RHID) that eventually leads to a conspicuous root hair bulge at the basal (root-tip oriented) end of the trichoblast (Grierson et al., 2014, Nakamura and Grebe, 2018). Several proteins accumulate at the RHID, most prominently, the Rho of Plants (ROP)/RAC small GTPases and their Guanine Nucleotide Exchange Factor (GEF) activators (Denninger et al., 2019). The second stage is tip growth. In addition to small GTPases, the cytoskeleton, the endomembrane trafficking machinery, cytoplasmic calcium, phosphoinositide lipids, hormones (e.g. auxin and ethylene) and reactive oxygen species are other major players in signaling pathways that modulate root hair development (Bascom et al., 2018a, Nakamura and Grebe, 2018).

The filamentous-actin (F-actin) and microtubule cytoskeletons orchestrate root hair development. The actin cytoskeleton in particular has been studied widely during tip

growth as it functions as tracks for the traffic of cellular cargo to the cell apex (Bascom et al., 2018a, Stephan, 2017, Szymanski and Staiger, 2018). Many insights into the role of the actin cytoskeleton in tip growth have been demonstrated through work with *Arabidopsis* mutants and pharmacological approaches involving the use of chemicals that disrupt F-actin. For example, the actin-disrupting compound, latrunculin B (LatB), inhibits tip growth, while also inducing the formation of root hairs and pollen tubes with irregular shapes (Bibikova et al., 1999, Gibbon et al., 1999). In this regard, *Arabidopsis* mutants with defects in the root hair-expressed vegetative *ACTIN2* (*ACT2*) gene are characterized by root hairs that mirror those treated with LatB (Ringli et al., 2002, Yoo et al., 2012). Furthermore, *ACT2* and *ACT7* mutants display an apical (shoot-ward) shift in the position of the RHID when compared to wild type (Kiefer et al., 2015).

To fulfill its cellular functions, the actin cytoskeleton is organized into higher order networks that correspond to the growth strategy of the cell. This is evident in tip-growing cells, whereby the base and shank of the cell consists mostly of thick, longitudinal F-actin bundles, while the apex contains actin fringes, rings, patches or a fine meshwork depending on the plant species or cell type (Stephan, 2017). To sustain tip growth, the integrity and organization of these tip-focused F-actin arrays must be maintained, a task that is facilitated by a diverse collection of actin-binding proteins and actin nucleators (Li et al., 2015, Paez-Garcia, 2018, Szymanski and Staiger, 2018).

The actin-related protein (ARP2/3) complex and its activator, suppressor of cAMP receptor (SCAR)-WASP family verprolin homologous (WAVE) complex (W/SRC-ARP2/3), is the best characterized actin nucleator in plants (Deeks and Hussey, 2005, Szymanski, 2005, Yanagisawa et al., 2013). The ARP2/3 complex consists of seven subunits that include the proteins ARP2, ARP3, ARPC1, ARPC2, ARPC3, ARPC4, and ARPC5, which were first identified in *Acanthamoeba* (Machesky et al., 1994). It was shown that the membrane-associated plant ARP2/3 complex has the same assembly mechanisms as the non-plant complexes (Kotchoni et al., 2009). Upon conversion from an inactive open conformation to an inactive closed conformation, the ARP2/3 complex promotes F-actin nucleation from the sides of existing filaments by forming a surface that mimics stable actin dimers (Blanchoin et al., 2000, Robinson et al., 2001, Rodal et al., 2005). Activation of ARP2/3 for efficient nucleation of F-actin requires the W/SCAR

nucleation promoting factor (NPF) complex. In addition to WAVE/SCAR, the NPF consists of the proteins SRA1, NAP1, ABIL and HSPC300/BRICK1 (BRK1) (Deeks et al., 2004, Djakovic, 2006, Frank and Smith, 2002, Jörgens et al., 2010, Le et al., 2006, Saedler et al., 2004). Studies of *Arabidopsis* trichome development have been most instrumental in revealing insights into the function of W/SCR-ARP2/3 in plants. Plant counterparts to the mammalian W/SCR-ARP2/3 subunits were first uncovered through the cloning of disrupted genes in a set of *DISTORTED* (*DIS*) *Arabidopsis* trichome mutants (Hülskamp et al., 1994, Mathur et al., 2003, Le et al., 2003, El-Assal Sel et al., 2004, Basu et al., 2004, Deeks et al., 2004, Zhang et al., 2005). W/SCR is the only known NPF for ARP2/3, and *BRK1* and *SCAR* mutants display null *arp2/3* trichome phenotypes (Le et al., 2006, Zhang et al., 2008). NPF activity of W/SCR to initiate an ARP2/3 actin nucleating response is also known to be positively regulated by ROP/RAC-GTP effector complexes (Basu et al., 2004, Uhrig et al., 2007). In *Arabidopsis* trichomes, active ROP/RAC-GTPase is coupled to W/SCR by the DOCK (dedicator of cytokinesis)-family GEF, SPIKE1 (SPK1) (Basu et al., 2008) (Yanagisawa et al., 2018).

In addition to trichome development, the W/SRC-ARP2/3 actin filament-nucleating module has been implicated in specifying leaf pavement cell shape, light and auxin-dependent root growth, stomatal gating, gravitropism, responses to salinity stress, and plant immunity (Li et al., 2003, Basu et al., 2005, Zhang et al., 2005, Dyachok et al., 2011, Zhao et al., 2013, Li et al., 2014, Zou et al., 2016, Isner et al., 2017, Badet et al., 2019, Pratap Sahi et al., 2018). The W/SRC-ARP2/3 complex has also been shown to play an essential role in some tip growing cells such as the protonemal cells of the moss *Physcomitrella patens*. This was shown when RNA interference (RNAi) of transcripts encoding selected subunits of the moss W/SRC-ARP2/3 complex resulted in substantial protonemal tip growth defects (Harries et al., 2005, Perroud and Quatrano, 2006, Finka et al., 2008). The importance of the W/SRC-ARP2/3 complex was further demonstrated by Perroud and Quatrano (2006, 2008) who showed that two of its components, BRK1 and ARPC4, accumulated in tips of moss protonemal cells. By contrast, *Arabidopsis* plants with mutations in components of the W/SRC-ARP2/3 complex displayed minimal or no defects in root hair and pollen tube growth (Li et al., 2003, Mathur et al., 2003),

140 and none of the subunits have been conclusively shown to exhibit clear polar
141 localization in these cell types. Therefore, the extent by which the W/SRC-ARP2/3
142 complex functions in tip growing cells of higher plants remains to be determined.
143 *SPIRRIG* (*SPI*) is one of eight genes that have been considered to be a member
144 of the *DIS* group, but compared to other *DIS* mutants, trichome phenotypes of *spi* are
145 less severe and the mutant does not display early stage cell swelling that is diagnostic
146 of the *DIS* group (Schwab et al., 2003). *SPI* was shown to encode a 3571 long amino
147 acid protein with N-terminally located armadillo (ARM) and concanavalin A (ConA)-like
148 lectin domains and C-terminally-located pleckstrin homology (PH), beige and Chediak
149 Higashi (BEACH) and WD40 repeat domains (Saedler et al., 2009). BEACH domain-
150 containing proteins are highly conserved in eukaryotes and are known to function in
151 membrane dynamics, vesicle transport, apoptosis and receptor signaling. This family of
152 proteins are of clinical importance as they have been implicated in a variety of human
153 disorders such as cancer, autoimmunity syndrome and autism (Cullinane et al., 2013).
154 In addition to mild trichome defects, *Arabidopsis SPI* mutants have short root
155 hairs characterized by fragmented vacuoles suggesting that SPI, like other eukaryotic
156 BEACH domain-containing proteins, functions in membrane trafficking (Saedler et al.,
157 2009). Additionally, an observation by Steffens et al. (2017) that showed SPI physically
158 interacting with proteins involved in endosomal sorting reinforces its role in membrane
159 remodeling. SPI was also demonstrated to associate with mRNA processing bodies (P-
160 bodies) suggesting a novel role for SPI in post-transcriptional regulation (Steffens et al.,
161 2015). Because *SPI* is one of the *DIS* genes, it was suggested that SPI might be
162 involved in actin-mediated cell developmental processes (Saedler et al., 2009), and
163 perhaps function in coordination with W/SCR and ARP2/3 complexes. However, SPI is
164 not a known W/SCR or ARP2/3 subunit; therefore, its relationship to ARP2/3 function is
165 unclear. Moreover, the uncertainty with regard to SPI function is confounded by the fact
166 that its subcellular localization in root hairs, which exhibit the most profound phenotype
167 when *SPI* is mutated, remains unknown. In this paper, we have addressed these
168 questions by showing that a functional SPI-fluorescent protein fusion accumulated at
169 the tips of rapidly growing root hairs. A SPI-tagged fluorescent protein fusion was not
170 detected in the RHID and in tips of non-growing mature root hairs. We further show that

171 the W/SCR complex subunits, BRK1 and SCAR2, localized to the RHID and exhibited
172 temporal dynamics opposite to that of SPI (i.e. functional fluorescent protein-tagged
173 BRK1 and SCAR2 declined as rapid root hair tip growth commenced). Double mutant
174 studies revealed that *SPI* and *W/SCR-ARP2/3* genetically interact suggesting that one
175 function of SPI is to modulate actin-dependent root hair development, in part through
176 pathways that overlap with W/SCR and ARP2/3 complexes.
177
178
179

RESULTS

Isolation of a New *SPIRRIG* Mutant Allele

We previously described a forward genetic screen that led to the isolation of three non-allelic recessive *Arabidopsis* mutants that were hypersensitive to the growth inhibitory effects of LatB. The *hypersensitive to LatB1* (*hlb1*) and *hlb3* mutants have been described previously (Sparks et al., 2016, Sun et al., 2019). *hlb1* was disrupted in a gene encoding a *trans*-Golgi Network-localized tetratricopeptide repeat protein involved in actin-mediated membrane recycling (Sparks et al., 2016), whereas the genetic lesion in *hlb3* was found to encode the class II actin nucleator formin (Sun et al., 2019). Here, we report on *hlb2*, the third of these recessive mutants. Like *hlb1* and *hlb3*, *hlb2* primary root growth was more severely inhibited by LatB when compared to wild type. In the absence of LatB or at low (i.e. 25 nM) LatB concentrations, the primary root length of *hlb2* was similar to wild type. Differences in root length between wild type and *hlb2* became apparent when seedlings were grown on a concentration of 50 nM LatB and higher (Supplemental Figure 1A and B).

Through map-based cloning, we found that the mutation in *hlb2* was confined to a region between the *AT1G02740* and *AT1G03410* loci. Nucleotide sequencing revealed that *hlb2* had a 10 base pair deletion (Chr1 position: 720,152 - 720,161) in exon 14 of the *AT1G03060* gene. This 10-base pair deletion led to an open-reading frame shift at the Asp^{1526} codon resulting in a truncated protein (Supplemental Figure 2A). *AT1G03060* encodes the BEACH domain-containing protein, SPI (Saedler et al., 2009) (Supplemental Figure 2A). Because the first *spi* mutant alleles were reported to have short root hairs (Saedler et al., 2009), we examined root hairs of *hlb2*. We found that *hlb2* had root hairs that were about 80% shorter than wild type with some root hairs forming only small bulges (Supplemental Figure 2B and C). Moreover, *hlb2* had mild trichome defects that were reminiscent of the phenotypes of previously isolated *spi* mutant alleles (Supplemental Figure 2D; Saedler et al., 2009). To further verify if *HLB2* is *SPI*, we obtained a mutant from the publicly available SALK collection (SALK_065311), which had a T-DNA insertion in the 10th exon of the *SPI* gene

211 (Supplemental Figure 2A; Alonso et al. (2003)). The SALK_065311 line we obtained is
212 the same as *spi-3* mutant allele reported previously in Steffens et al. (2015). In addition
213 to having similar root hair and trichome defects as *hlb2*, primary roots of *spi-3* were
214 hypersensitive to LatB (Supplemental Figure 2E), and a cross between *hlb2* and
215 SALK_065311 failed to complement each other in the F1 hybrid. Taken together, these
216 results indicate that *hlb2* is a new *spi* mutant allele. Based on earlier nomenclature
217 (Steffens et al., 2015), we renamed *hlb2* to *spi-5* (Supplemental Figure 2A). The *spi-5*
218 mutant allele was used for all subsequent experiments.
219
220 **SPIRRIG Localizes to the Tips of Rapidly Elongating Root Hairs**
221
222 SPI fluorescent protein fusions have been previously demonstrated to associate with P-
223 bodies and endosomes (Steffens et al., 2015, Steffens et al., 2017). However, these
224 constructs have not been shown to complement the defective root hair and trichome
225 phenotypes of *spi*. Because of the large size of SPI, we were unable to generate native
226 promoter-driven fluorescent protein fusions to the full length *SPI* complementary DNA or
227 genomic DNA. To overcome this problem, SPI was tagged with the 3x-Yellow
228 Fluorescent Protein (YFP) for energy transfer (YPet; Nguyen and Daugherty (2005))
229 using a method called recombineering. This method involves tagging the gene of
230 interest in the context of transformation-competent bacterial artificial chromosomes to
231 ensure that all regulatory sequences are included in the fluorescent protein fusion
232 (Brumos et al., 2020, Zhou et al., 2011).
233 Once *spi* was transformed with a recombineered *SPI-YPet* construct, primary
234 root hypersensitivity to LatB, short root hairs and defective trichome phenotypes were
235 rescued, indicating that the construct was functional (Figure 1A; Supplemental Figure
236 3). Transgenic complementation of *spi* with *SPI-YPet* provided additional evidence that
237 *HLB2* is *SPI*. Confocal microscopy revealed that SPI-YPet signal was strongest in the
238 tips of rapidly elongating root hairs (Figure 1B and C; Supplemental Movie 1). SPI-YPet
239 fluorescence was not detected or weak at the RHID and during early root hair bulge
240 formation, but intensified as root hairs transitioned to tip growth (Figure 1C;
241 Supplemental Movie 2). SPI-YPet signal dissipated as root hairs matured and tip growth

242 rate declined (Figure 1B and C; Supplemental Movie 3). A linear regression analysis
243 showed that the intensity of SPI-YPet fluorescence in root hair tips is significantly
244 positively correlated to rapid root hair growth (Figure 1D). These results indicate that the
245 SPI protein has functions related to root hair elongation and consistent with the short
246 root hair phenotypes of *spi*.
247
248 **SPIRRIG is Transported to the Root Hair Tip via Post-Golgi Vesicles**
249
250 The prominent SPI-YPet signal at the tips of elongating root hairs is reminiscent of the
251 localization patterns of post-Golgi markers such as RAB small GTPases, which are
252 known to function in tip-directed secretion (Preuss et al., 2004). We therefore
253 hypothesized that SPI is trafficked to the tips of root hairs via post-Golgi vesicles. To
254 test this hypothesis, seedlings expressing *SPI-YPet* were treated with brefeldin A (BFA).
255 BFA is a fungal toxin that is routinely used to investigate endomembrane dynamics
256 because it prevents vesicle formation for exocytosis by inhibiting ADP ribosylation factor
257 guanine nucleotide exchange factors (ARF-GEFs), while still enabling endocytosis and
258 some retrograde pathways to continue (Baluška, 2002, Doyle et al., 2015).
259 Consequently, BFA treatment causes the formation of endosomal agglomerations called
260 BFA bodies. Treatment of seedlings expressing *SPI-YPet* with 50 μM BFA induced the
261 formation of SPI-YPet agglomerates in root hairs (Figures 2A and B). The formation of
262 SPI-YPet fluorescent agglomerates was also observed in the root elongation zone
263 (Figure 2C). In the absence of BFA, SPI-YPet signal in the elongation zone was barely
264 detectable. However, upon exposure to BFA, bright fluorescent agglomerates of various
265 sizes became visible (Figure 2C). These results indicate that SPI-YPet is associated
266 with endomembranes and is trafficked to the root hair tips via BFA-sensitive post-Golgi
267 vesicles.
268 Inhibited root hair growth of *spi* and the formation of SPI-YPet agglomerates after
269 BFA treatment, suggest that *spi* may be defective in tip-directed protein secretion and
270 partly explain the short root hair phenotypes of *spi*. To address this question, we
271 expressed the secreted (SEC)-red fluorescent protein (RFP) in *spi* (Faso et al., 2009).
272 Similar to previous reports, rapidly elongating wild-type root hairs had a tip-focused

gradient of SEC-RFP (Sparks et al., 2016) (Figure 2D). By contrast, slow-growing root hairs of *spi* lacked these tip-focused SEC-RFP gradients (Figure 2E), thereby indicating defects in tip-directed bulk flow exocytosis.

SPIRRIG Maintains Root Hair Tip-Focused F-actin

In a study of other *spi* mutant alleles, the similarities in phenotypes between *spi* and *w/scr-arp2/3* suggests that SPI could function in actin-dependent cellular processes (Saedler et al., 2009). However, because trichome defects of *spi* were mild compared to other *w/scr-arp2/3* mutants, no obvious actin phenotypes were observed in *spi* trichomes (Schwab et al., 2003). To clarify the relationship between SPI and actin, we focused on investigating actin organization in root hairs since they displayed the most obvious growth defects in *SPI*-altered plants.

To study actin organization, we expressed the live F-actin reporter, *UBQ10: mGFP-Lifeact*, in *spi* (Vidali et al., 2010). This particular F-actin reporter was selected because it prominently labels the tip-focused F-actin meshwork typically observed in root hairs that are rapidly growing (Sparks et al., 2016). In wild type, fine F-actin networks were observed in the root hair bulge that had a weaker signal compared to the thicker actin bundles in other regions of the trichoblast (Figure 3A). As the root hair bulge expanded and the root hair transitioned to rapid tip growth, the tip-focused F-actin meshwork, which consisted of short filaments and dynamic puncta, became more conspicuous (Figures 3B-E; Supplemental Movie 4; Sparks et al. (2016)). When wild-type root hairs stopped elongating, the tip-focused F-actin meshwork was replaced with thick F-actin cables (Figure 3F).

F-actin organization in the tips of *spi* root hairs was different from that of wild type. As noted, some root hairs of *spi* were only able to form small bulges due to premature termination of tip-growth (Supplemental Figure 2). In *spi* root hairs, the distinct F-actin meshwork observed in wild-type root hairs was unable to form. Instead, F-actin in these *spi* root hair bulges contained thick F-actin cables that resembled those of wild-type root hairs that had terminated growth (Figure 3G and H). However, the thick F-actin cables in non-growing *spi*root hair bulges were unstable as they dissipated

(Figure 3I) and reformed again at a later time (Figure 3J). In the small population of *spi* root hairs that were able to undergo tip growth, a few exhibited the tip-focused F-actin meshwork that resembled those observed in elongating wild-type root hairs (Figure 3K). However, most of these slow growing *spi* root hairs lacked the tip-focused F-actin meshwork (Figure 3L and M; Supplemental Movie 4) or had thick F-actin bundles protruding to the tip, a feature that was reminiscent of non-growing, mature wild-type root hairs (Figure 3N). The disruption of the tip-focused F-actin meshwork in *spi* was quantified by measuring F-actin fluorescence from computer reconstructed transverse sections of the root hair tip and by taking the ratio of the average fluorescence over background signal. A higher ratio indicates a higher signal of tip-focused F-actin (Figure 3O). Our analysis showed that the fluorescence ratio in *spi* root hairs was significantly reduced compared to wild-type root hairs, supporting visual observations that the tip-focused F-actin meshwork in *spi* root hairs is disrupted (Figure 3P).

We next generated plants expressing both *SPI-YPet* and *mRuby-Lifeact* so we could simultaneously observe SPI and F-actin in growing root hairs. In elongating root hairs of dual labeled seedlings, SPI-YPet and the mRuby-labeled F-actin meshwork overlapped at the tip (Figure 3Q; Supplemental Movie 5). This provides support that root hair tip-localized SPI is associated with the tip-focused F-actin meshwork, and as such is involved in sustaining normal root hair elongation in coordination with actin.

BRK1 and SCAR2 are Molecular Determinants of the Root Hair Initiation Domain

The identification of *SPI* as one of the genes in the *DIS* group that also included genes encoding subunits of the W/SRC-ARP2/3 complex (Saedler et al., 2009) raises the possibility that SPI might function in root hair developmental pathways mediated by W/SRC-ARP2/3. Furthermore, the observation that SPI-YPET accumulation at the root hair tip (Figure 1) mirrors the enrichment of BRK1-YFP and APRC4-GFP at apex of *Physcomitrella* protonemal cells (Perroud and Quatrano, 2006, Perroud and Quatrano, 2008) raises the possibility that W/SRC-ARP2/3 maybe a root hair tip-localized complex. In an attempt to link SPI with the W/SCR-ARP2/3 complex, we imaged roots of *brk1* complemented with *BRK1promoter:BRK1-YFP* (from here on referred to as

335 BRK1-YFP) (Figures 4A-C) (Dyachok et al., 2008). Unlike SPI-YPet, we did not
336 observe a BRK1-YFP fluorescence gradient in rapidly elongating root hairs. However,
337 closer examination of trichoblasts revealed prominent BRK1-YFP signal at the plasma
338 membrane of the RHID that mirrored other known early root hair initiation site markers
339 such as ROP (Figure 4A). Unlike ROP, which had a persistent plasma membrane
340 localization throughout root hair development (Jones et al., 2002, Molendijk et al.,
341 2001), BRK1-YFP signal was transient and dissipated as root hairs transitioned to rapid
342 tip growth (Figure 4B; Supplemental Movie 6). This observation was in contrast to the
343 intensification of SPI-YPet fluorescence as root hairs proceeded with rapid tip growth
344 (see Figure 1). In agreement with our visual observations, a linear regression analysis
345 showed that BRK1-YFP fluorescence is inversely proportional to root hair growth rate
346 (Figure 4C).

347 Given that BRK1 stabilizes the entire family of SCAR proteins and is required for
348 functional W/SRC assembly (Le et al., 2006), we investigated if the SCAR protein
349 localized to the RHID, similarly to BRK1. To address this question, we imaged a
350 recombineered SCAR2-mCherry fusion expressed in the *scar1 scar2 scar3 scar4*
351 (*scar1234*) quadruple mutant. We found that like BRK1-YFP, SCAR2-mCherry marked
352 the RHID and dissipated when rapid root hair tip growth commenced (Figure 4D).

353 The accumulation of BRK1-YFP and SCAR2-mCherry at the RHID led us to
354 hypothesize that *brk1* and *scar1234* might have defects in root hair initiation. One
355 parameter that has been studied extensively as an indicator of root hair initiation defects
356 is planar polarity, which is a measure of root hair position along the length of the
357 trichoblast (Nakamura and Grebe, 2018). We found that root hair position of *brk1* and
358 *scar1234* shifted apically (i.e. toward the shoot) when compared to wild type (Figure
359 4F). The planar polarity defects of *brk1* was rescued by expressing *BRK1-YFP* in *brk1*
360 while partial complementation of *scar1234* was achieved by expressing *SCAR2-*
361 *mCherry* in *scar1234* (Figures 4E and F). Taken together, our results revealed that
362 BRK1 and SCAR2 are new molecular determinants of the RHID and are required for
363 specifying the position of root hair emergence.

364 Given that ARP2/3 is the known target of activated W/SRC, we hypothesized that
365 ARP2/3 might also localize to the RHID. To test this hypothesis, we imaged a line

expressing ARPC5-GFP, one of the subunits of the ARP2/3 complex (Yanagisawa et al., 2015). This line has been confirmed to complement the *arpc5* trichome defects. As reported previously, ARPC5-GFP labeled the plasma membrane of initiating trichome branches and the apex of elongating trichome branches (Yanagisawa et al. (2015); Supplemental Figure 4A and B). Nevertheless, when observed in root hairs, the ARPC5-GFP signal was distributed uniformly at various stages of development with no distinct accumulation at the RHID or root hair apex (Supplemental Figure 4C and D). Although there was no clear polarized localization of ARPC5-GFP in root hairs, it is possible that ARP2/3 is locally activated in RHID or root hair apex, but that active pool is obscured by a large soluble pool of the complex in this cell type.

SPI is Required for the Depletion of BRK1 as Root Hairs Transition to Tip Growth

Live cell microscopy of BRK1-YFP and SPI-YPet revealed contrasting spatial and temporal dynamics, with the former intensifying and the latter dissipating as root hairs elongated (Figure 1 and 4). To observe BRK1 and SPI simultaneously within the same root hair, we generated plants expressing both *SPI-YPet* and *BRK1-mRuby3*. Similar to BRK1-YFP, BRK1-mRuby3 labeled the RHID and dissipated as the root hair bulge expanded (Figure 5A). Within the same root hair cell, SPI-YPet fluorescence at the tip intensified as BRK1-mRuby3 dissipated (Figure 5A; Supplemental Movie 7). The depletion of BRK1 coinciding with the accumulation of SPI suggests that these proteins may be antagonistic to each other. To address this question, we expressed *BRK1-YFP* in *spi* and *SPI-YPet* in *brk1*. We found that unlike BRK1-YFP in the complemented *brk1* background (Figure 4B), BRK1-YFP signal in *spi* persisted throughout the entire imaging time course. In several cases, BRK1-YFP remained visible in non-growing root hair bulges of *spi* for more than 60 min (Figure 5B). The persistence of BRK1-YFP signal was also observed in short root hair outgrowths of *spi* (Figures 5C; Supplemental Movie 8). By contrast, SPI-YPet in *brk1* exhibited similar dynamics as SPI-YPet in the complemented *spi* (Figure 5D). In *brk1*, SPI-YPet signal was weak during early root hair bulge formation and intensified as root hair tip growth accelerated (Figure 5D). Taken

396 together, these results indicate that SPI is antagonistic to BRK1 during the transition
397 from root hair initiation to rapid tip growth.
398
399 **_SPI_ Genetically Interacts with _W/SRC-ARP2/3_ in Root Hairs**
400
401 The phenotypic overlap between *SPI* and *W/SCR*-and *ARP2/3* mutants suggest that
402 SPI participates in similar biological processes (Saedler et al., 2009). The polarized
403 localization of SPI, BRK1 and SCAR2 in root hairs observed here also indicate potential
404 functional relationships between SPI and W/SCR-ARP2/3 during root hair development.
405 However, it remains to be determined whether *SPI* genetically interacts with *W/SRC-*
406 *ARP2/3* pathway components. To address this question, we generated double *spi brk1*
407 mutants and compared their root hair phenotypes with single mutants. We first
408 investigated the genetic relationship between *SPI* and *BRK1* based on length of mature
409 root hairs. We found that at low magnification, root hair length of *brk1* appeared
410 morphologically similar to wild type (Figure 6A). Quantification of root hair length,
411 however, uncovered a small but significant reduction in root hair length in *brk1* when
412 compared to wild type (Figure 6B). On the other hand, *spi brk1* had short root hairs that
413 were similar to *spi* (Figure 6A and B). We next examined whether *SPI* and *BRK1*
414 genetically interact in specifying root hair planar polarity. We found that *spi* displayed a
415 more shoot ward (apical)-shifted root hair position when compared to wild type and
416 *brk1*. Quantification of root hair planar polarity showed that that root hair position of *spi*
417 was identical to *spi brk1* (Figure 6C). Taken together, our results indicate that *SPI* is
418 epistatic to *BRK1* for root hair planar polarity and tip growth.
419 Epistasis between *SPI* and *BRK1* prompted us to expand our genetic interaction
420 studies to other genes in the *ARP2/3* pathway. We therefore generated *spi arp2*, *spi*
421 *arp3* and *spi arpc5* double mutants and analyzed their root hair phenotypes. Like *brk1*,
422 root hairs of *arp2, arp3* and *arpc5* appeared to be morphologically similar to wild type
423 (Figure 7A; Supplemental Figure 5). Quantification of root hair length, however,
424 revealed slightly shorter root hairs in the single *arp2/3* mutants when compared to wild
425 type (Figure 7C), an observation consistent with the mild tip growth defects reported for
426 these mutants in the presence of the GFP:TALIN live cell probe for actin (Mathur et al.,

427 2003). On the other hand, *spi arp2*, *spi arp3* and *spi arpc5* appeared morphologically
428 hairless when viewed at low magnification (Figure 7; Supplemental Figure 5). This
429 observation was in contrast to *spi brk1* and *spi*, which had a number of short, but visible
430 root hair out growths spaced between hairless regions (Figures 6A, 7A, and 7BB;
431 Supplemental Figure 5). When viewed at high magnification we found that most of the
432 trichoblasts of *spi arp2*, *spi arp3* and *spi arpc5* had a high number of root hair bulges
433 that aborted tip growth soon after initiation (Figure 7B; Supplemental Figure 5).
434 Quantification of root hair length revealed that the joint contribution to the root hair
435 length phenotype made by combining *SPI* and *ARP2/3* complex mutations was greater
436 than an additive effect of *SPI* or *ARP* single mutations (Figure 7C). The enhancement of
437 the root hair length defect of *spi* by *arp2/3* single mutants indicate a synergistic
438 interaction between *SPI* and *ARP2/3* with regard to root hair tip growth.
439 We next investigated if *SPI* and *ARP2/3* genetically interact in specifying the
440 position of the RHID. We found a mild but statistically significant shoot ward shift in the
441 position of the RHID in *arp2*, *arp3* and *arpc5* when compared to wild type. The extent to
442 which the position of the RHID shifted towards the shoot in single *arp2/3* complex
443 mutants was less than that of *spi* and *brk1* (compare Figure 6C and 7D). On the other
444 hand, the position of the RHID in *spi arp2/3* was more similar to single *arp2/3* indicating
445 that *ARP2/3* is epistatic to *SPI* for root hair planar polarity (Figure 7C and D). In many
446 cases we observed that the aborted root hair bulges in *spi arp2/3* emerged very close to
447 the basal (root ward) end wall of the trichoblast (Figure 7C). The synergistic and
448 epistatic relationship between *SPI* and *ARP2/3*, for root hair length and planar polarity,
449 respectively, indicate that *SPI* also genetically interacts with *ARP2/3* during root hair
450 development. However, the nature of this interaction appears to differ from that of
451 *BRK1*.
452 Genetic interaction between *SPI* and *W/SRC-ARP2/3* was also analyzed for
453 other *spi* phenotypes such as primary root hypersensitivity to LatB (Supplemental
454 Figure 1). For LatB sensitivity, we found that *arpc5* primary roots were inhibited to the
455 same extent as wild type when grown on LatB (Supplemental Figure 6B). Although
456 primary roots of *arp2*, *arp3* and *brk1* exhibited some hypersensitivity to LatB, the
457 response of these mutants to the compound was not as severe as *spi* and leaned more

toward wild-type sensitivity. By contrast, the hypersensitivity of primary roots of *spi arp2*, *spi arp3*, *spi arpc5* and *spi brk1* to LatB was more similar to *spi* (Supplemental Figure 6A and B) suggesting genetic interactions also occurs between *SPI* and *W/SCR-ARP2/3* for this phenotype.

Genetic interaction between *SPI* and *W/SRC-ARP2/3* was also observed in trichomes (Li et al., 2003, Mathur et al., 2003, Schwab et al., 2003). Consistent with previous reports, *arp2*, *arp3*, *arpc5* and *brk1* had severe trichome shape defects when compared to wild type, while those of *spi* were mild when viewed with a scanning electron microscope. One particular trichome defect is branch length, in which *arp2*, *arp3*, *arpc5* and *brk1* trichomes have distinctively short branches when compared to wild type (Supplemental Figure 7). On the other hand, trichomes of *spi* were wavy and crooked, but not as short as those of *arp2*, *arp3*, *arpc5* and *brk1*. We found that trichomes of all the double mutants resembled those of *spi* (Supplemental Figure 7A). Quantification of branch length of all single and double mutants was consistent with visual observations, especially in showing that *spi brk1* and *spi arp2/3* resembled the branch length of *spi* (Supplemental Figures 7A and C). Our observations on trichome branch length provide additional evidence that *SPI* genetically interacts with *W/SRC-ARP2/3*.

482 **DISCUSSION**

483

484 Our work uncovers new insights underlying actin-mediated root hair development. A
485 major result from our studies is the revelation that SPI is a root hair tip-localized protein.
486 Although SPI fused to fluorescent proteins was reported to localize to endosomes and
487 P-bodies, such studies have been limited to transient expression assays in biolistically-
488 bombarded leaves (Steffens et al., 2015; Steffens et al., 2017). As such, a mechanistic
489 link between reported SPI subcellular localization patterns and cell growth phenotypes
490 (i.e. short root hairs and distorted trichome shapes) described in the original *spi* mutant
491 alleles has never been demonstrated. The large size of SPI and the possibility that it is
492 targeted to discrete cellular domains could have hindered transgenic complementation
493 and subsequent *in planta* localization efforts. Through our work, we have addressed this
494 knowledge gap and now show that a SPI-YPet fusion generated through
495 recombineering has complemented *spi* (Brumos et al., 2020, Zhou et al., 2011). In doing
496 so, we provide compelling evidence that SPI is a root hair tip–enriched BEACH domain-
497 containing protein.

498 Our studies indicate that SPI mediates root hair tip growth by maintaining the tip-
499 focused fine F-actin meshwork, although the precise mechanism by which this is
500 accomplished is unknown. The root hair tip-focused F-actin meshwork is the functional
501 equivalent of domain-specific actin structures found in other tip-growing cells such as
502 cortical actin fringes in pollen tubes and actin spots in moss protonemata (Bascom et
503 al., 2018a). Although the tip-focused F-actin meshwork was able to form in a population
504 of *spi* root hairs, it often dissipated or was replaced by thick actin cables, a feature of
505 mature wild-type root hairs that are terminating tip growth. The root hair phenotypes and
506 corresponding depletion of tip-focused F-actin in *spi*is reminiscent of studies of BEACH
507 domain-containing proteins in mammalian cells, particularly in neurons, which have
508 often been compared to tip-growing plant cells (Baluška, 2010). For instance, neuronal
509 dendritic spines are cytoplasmic protrusions that modulate excitatory synaptic
510 transmission in the mammalian nervous system. Actin is a major component of dendritic
511 spines and it plays a central role in driving the dynamic shape changes and secretory
512 activities of these cytoplasmic protrusions during synaptic signaling (Cingolani and

513 Goda, 2008). In animals, neurobeachin (Nbea) is a BEACH domain-containing protein
514 that has a similar domain architecture as SPI. Cultured neurons of *Nbea* mice
515 knockouts had fewer dendritic spine protrusions and depleted F-actin at the synapse
516 (Niesmann et al., 2011). Another BEACH domain-containing protein called FAN was
517 shown to be crucial for the formation of filopodia, actin-rich plasma membrane
518 extensions that enable motile cells to probe their environment (Mattila and Lappalainen,
519 2008). FAN deficient fibroblasts had reduced filopodia formation and were unable to
520 reorganize their actin cytoskeleton in response to upstream activation by tumor necrosis
521 factors (Haubert et al., 2007). Taken together, these results indicate that actin-mediated
522 regulation of polarized cell growth by BEACH domain-containing proteins is likely to be
523 conserved across animals and plants.
524 The formation of SPI-YPet agglomerates in response to BFA indicates that SPI is
525 associated with post-Golgi vesicles. This result is consistent with observations made
526 with BEACH domain-containing proteins in mammals. For example, Nbea was shown to
527 localize to vesicular endomembranes adjacent to the *trans*-Golgi network, and like SPI,
528 the distribution of Nbea-positive post-Golgi vesicles was altered by BFA (Wang et al.,
529 2000). Furthermore, the *Caenorhabditis elegans* Nbea homolog, SEL-2, was
530 demonstrated to function in endomembrane traffic in polarized epithelial cells based on
531 the finding that *sel-2* mutants mistarget proteins normally found in the apical cell surface
532 to the basolateral surface (de Souza et al., 2007). Here, the protein secretory marker
533 SEC-RFP, which is typically trafficked to the tips of elongating wild-type root hairs
534 (Sparks et al., 2016), was uniformly distributed in *spi* root hairs. The absence of tip-
535 directed SEC-RFP gradients in *spi* root hairs shows that, as in mammals, plant BEACH
536 domain-containing proteins are required for proper targeting of molecular cargo to
537 points of polarized cell growth.
538 Another significant result from our studies is the discovery that BRK1 and SCAR2
539 are molecular determinants of the RHID. The localization of BRK1 and SCAR2 to the
540 RHID and their dissipation as root hair tip growth commenced, contrasts with findings in
541 *Physcomitrella* in which a functional BRK1-YFP distinctly labeled the tips of caulonemal
542 cells (Perroud and Quatrano, 2008). Like BRK1-YFP, an ARPC4-GFP construct labeled
543 the tips of caulonemal cells (Perroud and Quatrano, 2008) whereas no clear tip-focused

544 labeling of ARPC5-GFP was observed in root hairs. The observation that BRK1-YFP
545 prominently localized to the RHID, but dissipated during active root hair tip growth was
546 surprising given that the *Arabidopsis BRK1* complemented the defective filamentous
547 growth of *Physcomitrella BRK1* knockouts (Perroud and Quatrano, 2008). This suggest
548 that seed plants might have evolved a specialized function for the W/SCR-ARP2/3
549 complex in which it acts predominantly at the site of root hair emergence and early
550 bulge formation with only a minor role in driving actin-dependent tip growth. The fact
551 that *Physcomitrella BRK1 and ARPC4* mutants have clear tip growth defects, while
552 *Arabidopsis W/SCR-ARP2/3* mutants have only weak to no tip growth abnormalities,
553 supports this possibility (Le et al., 2003, Mathur et al., 2003, Perroud and Quatrano,
554 2006, Perroud and Quatrano, 2008). By contrast, knockouts of an *Arabidopsis SPI*
555 orthologue in the liverwort, *Marchantia polymorpha*, led to short rhizoids indicating
556 conserved functions of SPI across land plants in regulating tip growth (Honkanen et al.,
557 2016). In other single cell types such as diffusely-growing trichomes, W/SCR-ARP2/3
558 subunits likely play a more prominent role than SPI based on their more severe
559 trichome phenotypes when expression of their encoding genes are suppressed.
560 However, the epistatic relationships between *SPI* and *W/SCR-ARP2/3* for trichome
561 morphology and primary root hypersensitivity to LatB as reported here continue to point
562 to functional relationships between these genes in diffusely-growing cells. The
563 observation that phenotypes of *spi w/scr-arp2/3* tilt more toward *spi* indicate that SPI
564 might negatively regulate an actin pathway that is parallel to ARP2/3.
565 The weakening of BRK1-mRuby3 fluorescence coinciding with SPI-YPet
566 accumulation, and the persistence of SPI-YPet signal in *spi* root hair tips, provides
567 indirect evidence that SPI might play a role in mediating BRK1 stability or localized
568 clustering at the plasma membrane of the RHID. Because *spi brk1* root hair phenotypes
569 resemble *spi*, ectopic expression of BRK1 does not appear to contribute to the *spi*
570 phenotypes. Although, it is unknown why BRK1-YFP signal persists in *spi*, it is tempting
571 to speculate that SPI might modulate BRK1 via protein degradation pathways. This
572 possibility is supported by studies in mammals pointing to a role for BEACH domain-
573 containing proteins in protein degradation via the ubiquitination pathway. In mouse
574 models for example, the BEACH domain-containing protein, WDR81, was shown to be

575 essential for removal of autophagy-dependent ubiquitinated proteins (Liu et al., 2017).
576 In this regard, it is worth noting that the W/SCR-ARP2/3 complex was demonstrated to
577 function in stress-induced autophagy (Wang et al., 2016) and proteasome inhibitors
578 stabilized SCAR during dark-induced primary root growth inhibition (Dyachok et al.,
579 2011). It is possible that SPI-mediated proteolytic pathways and BRK1 operate
580 antagonistically to specify the levels of W/SCR at the RHID that enables the transition to
581 actin-dependent rapid tip growth. However, such as scenario is complicated by the
582 observation that the formation of tip-directed SPI-YPet does not appear to require
583 BRK1. This suggest that SPI's appearance at the root hair tip is regulated by other
584 factors besides W/SCR.

585 The functional links between SPI and W/SCR-ARP2/3 during root hair
586 development as suggested by live cell imaging is supported by the double mutant
587 studies reported here. We found that *SPI* is epistatic to *BRK1* for RHID and root hair tip
588 growth. For *SPI* and *ARP2/3*, synergistic and epistatic genetic interactions were
589 observed for root hair tip growth and root hair planar polarity, respectively. Synergistic
590 genetic interactions can arise when converging pathways are disrupted (Pérez-Pérez et
591 al., 2009), and the severe root hair phenotypes of *spi arp2/3* double mutants may reflect
592 parallel pathways that are involved in actin-dependent root hair tip growth. The
593 detection of synergistic genetic interactions in root hairs with *ARP2/3* mutants, but not
594 with *brk1* is unexpected as *brk1* is null for W/SRC-dependent ARP2/3 activation (Le et
595 al., 2006), and W/SRC is the only known ARP2/3 activator in *Arabidopsis* (Zhang et al.,
596 2008). These genetic data may reflect the existence of an unknown ARP2/3 activator or
597 an NPF-independent function of ARP2/3. Future studies will probe deeper into the
598 regulatory relationships between *SPI* and *W/SCR-ARP2/3* that underlie these
599 unexpected genetic interactions.

600 In summary, our work provides new data that contribute to our understanding of
601 actin-mediated root hair development. A crucial result from our work is the discovery
602 that SPI and the W/SCR subunits, BRK1 and SCAR2, exhibit polarized localization
603 patterns in root hairs that point to potential functional relationships among these
604 proteins during root hair development. Based on our cell biological studies, we propose
605 a model for which new hypotheses can be tested (Figure 8). We propose that a RHID-

606 localized ROP/RAC-GTPase (Jones et al., 2002, Molendijk et al., 2001) activates
607 W/SCR during root hair initiation in a manner that mirrors that of the DOCK family GEF,
608 SPK1, which was shown to occur during trichome morphogenesis (Basu et al., 2008).
609 Although the precise ROP-based machinery that facilitates this process during root hair
610 development has yet to be determined, ROP-GEF3 could be the functional equivalent of
611 SPK1 given that it localizes to the RHID (Denninger et al., 2019) in a manner similar to
612 BRK1 and SCAR2. Although epistatic and synergistic genetic interactions presented in
613 our double mutant studies support the occurrence of overlapping pathways between
614 *SPI* and *W/SCR-ARP2/3*, the precise nature of such relationships remain unclear. One
615 plausible scenario is that SPI negatively regulates an actin pathway that is parallel to
616 W/SCR-ARP2/3. The persistence of BRK1-YFP signal in *spi* suggests that one
617 mechanism for negative regulation could occur at a node in which SPI and W/SCR
618 converge. For the future, it will be important to determine whether SPI physically
619 interacts with actin or subunits of the W/SCR-ARP2/3 complex to better explain the
620 functional links between SPI and W/SCR-ARP2/3.
621
622

623 **METHODS**

624

625 **Forward-Genetic Screening and Map-Based Cloning**

626

627 The *hlb* mutants from which the *spi-5* mutant allele was identified were isolated from a
628 population of Transfer-DNA (T-DNA) seed (Arabidopsis Biological Research Center
629 stock CS31100). Plants from which the seeds were derived from were transformed with
630 the activation tagging pSKI015 plasmid (Weigel et al. 2000; Sparks et al., 2016; Sun et
631 al., 2019). Briefly, mutagenized seeds were surface sterilized in 95 % (v/v) ethanol and
632 20% bleach (v/v), followed by three washes in sterile deionized water. A solution of 0.5
633 x Murashige and Skoog (MS) basal salt medium with vitamins (PhytoTech Labs, USA)
634 and 1 % (w/v) sucrose was prepared, and the pH of the solution was adjusted to 5.7.
635 After adding 0.5% agar (w/v) (Sigma-Aldrich), the solution was autoclaved and allowed
636 to cool to room temperature. Upon reaching 55ºC, a stock solution of 10 mM LatB
637 (CalBiochem-EMD Chemicals) in 100% Dimethyl Sulfoxide (DMSO) was added to make
638 a final LatB concentration of 100 nM. Sterilized seeds were suspended in the MS-agar-
639 LatB medium and gently swirled to evenly distribute the seed. The seed-MS-agar-LatB
640 mixture was poured to a thickness of 2 mm on the base of 10 cm x 10 cm Petri dishes.
641 After keeping plates at 4ºC for 48 h, they were positioned vertically in a Conviron set to
642 24°C with a 14 hours light (120 µmol $m^{-2}s^{-1}$)/ 10 hours dark cycle. Six days after transfer
643 to the Conviron growth chamber, seedlings that exhibited severe growth inhibition were
644 transplanted to LatB-free media and grown to maturity.

645 For LatB hypersensitivity assays, seed from selected plants and the *hlb2* mutant
646 were planted on the surface of a 3 mm layer of polymerized 0.5 x MS - 1% agar growth
647 media in gridded square 10 cm × 10 cm Petri plates and grown in the same Conviron
648 used for screening. Four-day-old seedlings with primary roots that were about 1 cm long
649 were selected. Selected seedlings were transplanted to a new set of square Petri dishes
650 containing MS medium supplemented with 50 nM LatB or MS supplemented with the
651 appropriate volume of LatB solvent (i.e. DMSO). During transplant, the tip of the root
652 was positioned at the grid line of the Petri dish and maintained in a vertical orientation.
653 Four days after transplanting, images of the roots were captured with a Nikon Insight

654 digital camera mounted on a copy stand. Primary root length was expressed as the
655 distance between the position of the root tip 4 days after transplant and the grid line
656 where the root tip was positioned during transplant (Supplemental Figure 1).
657 To identify the *HLB2* gene, homozygous *hlb2* (Col-0 ecotype) was out-crossed to
658 the Landsberg *erecta* ecotype to generate seeds for map-based cloning because
659 attempts to identify the responsible mutation for *hlb2* phenotype using TAIL-PCR had
660 been unsuccessful. Segregating F2 seedlings were surface sterilized as described
661 above and grown for three days. These seedlings were then transferred to MS media
662 containing 50 nM LatB and root lengths were marked on the plates to track root growth.
663 Transferred seedlings were grown vertically for an additional four days in the growth
664 chamber and seedlings that showed root hypersensitivity to 50 nM LatB were selected
665 for mapping. Briefly, DNA was extracted (Edwards et al., 1991) from about 2600 LatB
666 sensitive seedlings and cloned with simple sequence length polymorphism (SSLP) and
667 cleavage of amplified polymorphic site (CAPS) markers to chromosome one between
668 *AT1G02740* and *AT1G03410* loci (Lukowitz et al., 2000), which spanned 248 kb with 77
669 annotated genes. Primers were then designed to several candidate genes based on
670 the sequenced 248 kb region. Nucleotide sequencing revealed that *hlb2* mutation had a
671 10 base pair deletion (Chr1 position 720,152- 720,161) in exon 14 of the *AT1G03060*
672 gene. In addition, we obtained a T-DNA insertional mutant (SALK_065311) from the
673 ABRC with predicted insertion in *SPI*. After genotyping, SALK_065311 was subjected to
674 similar LatB hypersensitivity and growth assays as *hlb2* as aforementioned. Allelism
675 was determined by examining the F1 progeny from a cross between *hlb2* ×
676 SALK_065311. Following the nomenclature of Steffens et al. (2015), SALK_065311 and
677 *hlb2* were named *spi-3* and *spi-5*, respectively.
678

679 **Generation of Fluorescent Protein-Tagged Constructs and Plant Lines**

680

681 The SPI protein was tagged at the C-terminus with the fluorescent protein 3x-YPet by
682 the recombineering method (Zhou et al., 2011). *Agrobacterium tumefaciens* UIA143
683 pMP90 harboring a SPI-YPet recombineering construct was used to transform the *spi-5*
684 mutant by the floral dip method (Clough and Bent, 1998). Transgenic lines were isolated

685 based on resistance to kanamycin and restoration of wild-type root length. Presence of
686 the SPI-YPet transgene was amplified with primers (5'-
687 ATTCCACAAGCAACCAGTCAC-3' and 5'-AACAGAGTTGAGAGTGGCTCG-3') and
688 sequenced to confirm the correct configuration. Final validation of *SPI-YPet* expression
689 was accomplished by screening selected lines under the confocal microscope for YPet
690 fluorescence and complementation of the short root hair phenotype.
691 *SCAR2-mCherry* lines were also generated by recombineering in which an
692 mCherry tag was fused to an internal region of SCAR2 (Sharan et al., 2009). The
693 mCherry tag was inserted after amino acid 585 in SCAR2 to generate SCAR2-
694 i2mCherry. Recombineering primers were designed as follows: the forward primer
695 contained 50 SCAR2 nucleotides upstream from the insertion site of SCAR2 and 18
696 nucleotides of the 5' end of the mCherry cassette, which had a 5x Glycine, 1 Alanine
697 linker. The reverse primer contained 50 nucleotides after the insert site of SCAR2 and
698 24 nucleotides of the 3' end of the mCherry cassette. The JAtY75L14 clone was
699 transformed into the recombineering competent *E.coli* strain SW105 and recombined
700 with the SCAR2-i2mCherry recombineering cassettes. A flippase recombination
701 reaction removed the ampicillin resistance marker. The sequence between the two test
702 primers was verified by DNA sequencing. The clones were transformed into
703 *Agrobacterium* and then into *scar1234* plants (Dyachok et al., 2008). Because both
704 *scar1234* plants and the recombineering clones were Basta resistant, plants on MS
705 plates were screened by eye for rescued trichome phenotypes. Rescued plants were
706 genotyped with the recombineering test primers and screened for fluorescence with a
707 confocal microscope.
708 The *BRK1promoter: BRK1-YFP* introduced into the *brk1-1* mutant and *ARPC5-*
709 *GFP* are described in Dyachok et al. (2008) and Yanagisawa et al. (2015), respectively.
710 For the *BRK1-mRuby3* construct, the fluorescent protein 3x-mRUBY3 was tagged with
711 a C-terminal linker (10 Alanine, Glycine) using Thermo Fisher Scientific GeneArt to
712 include BamH1 and XbaI sites at its 5' and 3' ends, respectively. Codon optimization for
713 *Arabidopsis* was performed on the 3x-mRUBY3 and internal linkers prior to synthesis.
714 The 3X-mRuby3 fragment was inserted as a BamH1/XbaI into the plasmid
715 *pBRK:YFPpEZRK* (Dyachok et al., 2008).The *Agrobacterium* floral dip method (Clough

716 and Bent, 1998) was used to transform *brk1-2* plants, and transformation was confirmed
717 when this construct fully restored defective *brk1-2* trichomes.
718 Plants expressing *BRK1-YFP* were crossed with *spi-5* to generate *BRK1-YFP* in
719 *spi-5* lines. In parallel, plants expressing *SPI-YPet* were crossed with *brk1* to obtain SPI-
720 YPet in *brk1* lines. *Spi-5* was directly transformed with the *UBQ10:mGFP-Lifeact*
721 construct by the floral dip method (Clough and Bent, 1998). *Spi-5* expressing SEC-RFP
722 was generated by crossing *spi-5* with *SEC7-RFP*-expressing wild-type plants and
723 progeny in subsequent generations that exhibited fluorescence and the *spi* root hair
724 phenotypes were selected for analysis.
725
726 **Generation of Double Mutants and Dual Fluorescent Protein-Labeled Plant Lines**
727
728 *Arp2* (SALK_077920), *arp3* (SALK_010045), *arpc5* (SALK_123936) and *brk1-1*
729 (Djakovic, 2006, Le et al., 2006, Li et al., 2003) were crossed with *spi-5* to generate
730 double mutants. Single mutants were obtained from the ABRC and genotyped to verify
731 zygosity. Progeny from crosses were genotyped for the presence of the double mutation
732 by PCR-based approaches using the primers: ARP2LP 5'-
733 CGCTTTTTACTCCGGTAAACC-3' ARP2RP 5'-CATGCAGTAGAAGGAAGCTGG-3'
734 ARP3LP 5'-AATTGCTGGCAAAGATGTCAC-3' ARP3RP 5'-
735 AGCTCTTCGTGTGTCAATTGG-3' ARPC5LP 5'-TGCAAATTCCACCAAATCTTC-3'
736 ARPC5RP 5'-CTTTTGAAATGGTCAAATGGC-3'. The *spi-5* mutation in the double
737 mutants was confirmed using primers SPIF 5'-CAGTTACGAGGATCTTAGTCTTTC-3'
738 and SPIR 5'-CCAGTCCAGAAGGACATGTTC-3'. For *brk1-1*, which had a single base
739 pair deletion (Djakovic, 2006), PCR products were amplified using BRK1F 5′-
740 TTGAATCGAAAAAGGGCGAAT-3′ and BRK1R 5′-CGAAATCGAGAAAACTCCAAAA-3′
741 and the resulting fragment was sequenced to ensure deletion using the BigDye
742 Terminator chemistry (v3.1, Thermo Fisher Scientific) on an ABI3730XL DNA
743 sequencer (Thermo Fisher Scientific) following the manufacturer's instruction.
744 To generate plant lines co-expressing *SPI-YPet* and *BRK1-mRuby3*, *SPI-YPet* in
745 *spi-5* was crossed with *BRK1-mRuby3* in *brk1-2*. Progeny from subsequent generations
746 that exhibited yellow and red fluorescence and rescued root hair and trichome

phenotypes were selected for analysis. For lines expressing *SPI-YPet* and *mRuby3-Lifeact* (Bascom et al., 2018b), *SPI-YPet* in *spi-5* was directly transformed with a *UBQ10:Lifeact-mRuby3* construct. Seedlings that showed both YPet and mRuby3 fluorescence were selected under the confocal microscope.

Evaluation of Root Hair Length and Planar Polarity

Seeds of mutants were surface-sterilized in ethanol and bleach as described above. To evaluate root hair length and planar polarity, seeds were planted on 48 × 64 mm coverslips coated with 0.5 x MS, 1% sucrose and 0.4 % (w/v) Gelzan ™ CM (Sigma Aldrich, USA) according to Dyachok et al. (2016). Coverslips were placed in 9 cm round Petri dishes and stratified in 4ºC for 48 h. After stratification, the coverslip system with planted seed were kept in a 24°C growth chamber with 14 hours light (120 µmol $m^{-2}s^{-1}$)/ 10 hours dark cycle for 5 to 6 days.

To quantify root hair length, fully-grown root hairs from a region of the primary root located between 5 to 15 mm from the root tip were photographed with a Nikon SMZ1500 stereomicroscope. For planar polarity measurements, images of trichoblasts in which the apical and basal end walls were clearly visible were acquired with a Nikon Eclipse TE300 inverted microscope using a 20x objective. Root hair lengths were extracted from digital images using ImageJ (v1.51) software (https://imagej.nih.gov/ij/). For planar polarity, the distance between the basal trichoblast wall and base of the emerging root hair (a) and the length of the trichoblast (b) were obtained using Image J. The ratio of a/b was used as an indicator of relative root hair position with a value of 0 indicative of root hairs emerging at the basal-most end of the trichoblast and 1 indicative of root hairs emerging at the apical-most end of the trichoblast (Fischer et al., 2006). Box and violin plots were drawn on R software (R Core Team, 2019) using ggplot function in ggplot2 package (Wickham, 2016). Two-way Analysis of Variance (ANOVA) statistical analysis and Tukey's post-hoc tests were performed on R software (R Core Team, 2019) using car (Fox and Weisberg, 2019) and agricolae (de Mendiburu, 2020) packages. Pairwise non-parametric Kolmogorov-Smirnov tests were done using ks test function available in the basic package (R Core Team, 2019).

778

779 **Microscopy and Image Analysis**

780

781 Live cell imaging of root hairs using confocal microscopy was performed on 4 or 5-day-
782 old seedlings grown on the 48 mm × 64 mm coverslip system described above.
783 Coverslips with the seedlings were placed horizontally on the stage of an inverted Leica
784 SPX-8 point scanning confocal microscope (Leica Microsystems, Buffalo Grove, Illinois)
785 or an UltraView ERS spinning-disc confocal microscope (Perkin Elmer Life and
786 Analytical Sciences, Waltham, Massachusetts) equipped with 40 × water (numerical
787 aperture=1.10) or 100 × oil (numerical aperture=1.40) immersion objectives. SPI-YPet
788 and YFP-BRK1 were imaged by illuminating roots growing along the coverslip surface
789 with the 514 nm line of the SPX-8 Argon laser and emission detected at 527 nm.
790 Images of root hairs expressing SCAR2-mCherry, BRK1-mRuby3, Lifeact-mRuby and
791 SEC7-RFP were acquired through illumination with the tunable SP8-X white light laser
792 (560-580 nm) and detecting emission at 610 nm. Excitation and emission parameters
793 for GFP (GFP-ARPC5 and mGFP-Lifeact) were 488 nm and 510 nm, respectively.
794 Time-lapse movies or single time point images were collected using Volocity acquisition
795 version 6.3.5 (Improvision) or SPX-8 LAS software, for the UltraView and Leica SP8-X,
796 respectively.
797 Quantification of fluorescence from root hair images was conducted on 8-bit
798 confocal images acquired at a single fixed focal plane that spanned the median of the
799 cell (SPI-YPet, BRK1-YFP and SEC-RFP) or from maximum projected images (mGFP-
800 Lifeact). For SPI-YPet and SEC-RFP, an oval region of interest (ROI) at the root hair tip
801 was drawn and mean fluorescence within this area was acquired using Image J.
802 Fluorescence was expressed as the ratio of mean fluorescence within the root tip ROI
803 to background fluorescence. For SPI-YPet, the background used was the region
804 adjacent, but outside the root hair tip (Figure 1C) while for SEC-RFP, the background
805 used was an area on the sub-apical region of the root hair tip (Figure 2F). For BRK1-
806 YFP, a ROI was drawn along the apical-most root hair tip that was about 20 pixels-wide
807 using the selection brush tool of image J. The ratio of fluorescence within this area to
808 background fluorescence was obtained (Figure 2C). Root hair growth rate data was

809 derived from the same root hair images in which fluorescence images were acquired.
810 For the former, an image of a root hair was taken at time 0 and every 5 minutes
811 thereafter. The growth rate refers to the displacement of the root hair tip in μm divided
812 by time elapsed (min).
813 To quantify tip-focused F- actin, 25 optical sections were taken at 0.5 μm
814 intervals using the UltraView spinning-disc confocal microscope. Raw Ultraview Z-
815 stacks were exported to Imaris image analysis software version 9.2.0 (Bitplane).
816 Transverse sections of the root hair tip were obtained from Z-stacks using the surpass
817 view interface of the Imaris software and exported as 8-bit TIFF files. From these
818 images, an ROI spanning the circular area of the root hair tip was drawn using image J
819 and mean fluorescence was extracted (Figure 3O). The ratio of the tip fluorescence to
820 background was obtained from 18- 21 root hairs.
821 For SPI-YPet and BRK1-YFP, a scatter plot to determine the relationship
822 between growth rate and tip-focused fluorescence was done in R (R Core Team, 2019)
823 using ggplot function in ggplot2 package (Wickham, 2016). Linear regression analysis
824 were performed using lme4 package on R software (Bates et al., 2015, R Core Team,
825 2019).
826 Trichomes were imaged using a Hitachi Table top TM3000 scanning electron
827 microscope or with a Nikon SMZ 1500 stereo microscope. Images of trichomes from
828 newly emerging leaves of 3-week-old plants were collected and branch length was
829 measured using Image J.
830
831 **Accession Numbers**

832 Sequence data from this article can be found in the Arabidopsis Genome
833 Initiative or GenBank/ EMBL databases under the following accession numbers: *SPI*
834 (AT5G61350), *BRK1* (AT2G22640), *ARP2* (AT3G27000), *ARP3* (AT1G13180), *ARPC5*
835 (AT4G01710), *SCAR1* (AT2G34150), *SCAR2* (AT2G38440), *SCAR3* (AT1G29170),
836 *SCAR4* (AT5G01730)

837
838 **Supplemental Data**

Supplemental Figure 1. Primary Root Growth of *hlb2* Seedlings is Hypersensitive to LatB.

Supplemental Figure 2. *HLB2* Encodes the Beach Domain Containing Protein, SPIRRIG.

Supplemental Figure 3. *SPI-YPet* construct complements *spi*

Supplemental Figure 4. ARPC5-GFP is localized uniformly in the cytoplasm of developing root hairs.

Supplemental Figure 5. Root hair phenotypes of *spi arp2/3* mutants

Supplemental Figure 6. *SPIpro:SPI-YPet* complements the primary root hypersensitivity to LatB, short root hair and distorted trichome phenotypes of *spi*.

Supplemental Figure 7. Distorted trichome defects of *spi arp2*, *spi arp3*, *spi arpc5* resemble *spi*.

Supplemental Movie 1. Time-Lapse Confocal Microscopy of SPI-YPet in a Rapidly Elongating Root Hair.

Supplemental Movie 2. Time-Lapse Confocal Microscopy of SPI-YPet in a Root Hair Bulge Transitioning to Tip Growth.

Supplemental Movie 3. Time-Lapse Confocal Microscopy of SPI-YPet in a Root Hair during Termination of Tip Growth.

Supplemental Movie 4. Spinning-Disc Confocal Microscopy of Lifeact-mGFP in Elongating Root Hairs of Wild type and *spi*.

Supplemental Movie 5. Spinning-Disc Confocal Microscopy of a Rapidly Elongating Root Hair Co-Expressing SPI-YPet and mRuby3-Lifeact.

Supplemental Movie 6. Time-Lapse Confocal Microscopy of BRK1-YFP Root Hair Bulge Transitioning to Tip Growth.

Supplemental Movie 7. Time-Lapse Confocal Microscopy of a Root Hair Bulge Transitioning to Tip Growth and Co-Expressing SPI-YPet and mRuby3-Lifeact.

Supplemental Movie 8. Time-Lapse Confocal Microscopy of a *spi* Root Hair Expressing BRK1-YFP.

Supplemental Table 1. Statistical results for non-parametric Kolmogorov- Smirnov test for data in Figure 7C on root hair length in wild-type, *spi*,*arp and spi arp*

Supplemental Table 2. Statistical results for non-parametric Kolmogorov- Smirnov test for data in Figure 7D on root hair planar polarity in wild-type, *spi*, *arp and spi arp*.

ACKNOWLEDGMENTS

We thank Drs. Jose Alonso and Anna Stepanova (North Carolina State University) for assistance with recombineering and Dr. Magdalena Bezanilla (Dartmouth College) for the Lifeact-mRuby construct. This work was supported by the National Aeronautics and Space Administration (NASA grants 80NSSC19K0129 and 80NSSC18K1462) and the Noble Research Institute to E.B.B.) and by the National Science Foundation (NSF MCB Grant No.1121893) to D.B.S. We also thank Dr. Larry M. York (Noble Research Institute) and Dr. Wayne Versaw (Texas A.M. University) for critical comments on the manuscript.

AUTHOR CONTRIBUTIONS

899 S.C., T.K, D.B.S and E.B.B. conceptualized and designed the research, and analyzed
900 and interpreted the data. S.C., J.A.S. and E.B.B. conducted root hair, primary root
901 growth and trichome assays, microscopy, image and statistical analysis of data. T.K.,
902 J.A.S., B.R.K., E.L.M. and D.B.S. generated various research reagents. All authors
903 contributed to writing the manuscript.
904
905 **FIGURE LEGENDS**
906 **Figure 1.** A Functional SPI-YPet Fusion Localizes to the Tips of Growing Root Hairs.
907 **(A)** SPI-YPet rescues the short root hair phenotype of *spi*. Bar = 100 μm.
908 **(B)** Low magnification image shows that SPI-YPet signal is most prominent at the tips of
909 rapidly expanding root hairs (arrows). SPI-YPet signal is weak during initiation/early
910 bulge formation and mature root hairs that have terminated tip growth (**). Bar = 50 μm
911 **(C)** High magnification images of single root hairs during bulge formation until tip growth
912 termination. SPI-YPet is enriched at the tip of root hairs that are rapidly growing or
913 transitioning to tip growth. Faint SPI-YPet signal is found in bulging root hairs or those
914 that have stopped elongating (**). Bar = 10 μm.
915 **(D)** Scatter plot showing correlation analysis of root hair tip SPI-YPet fluorescence and
916 root hair tip growth. The mean fluorescence in the oval in region 1 divided by the oval in
917 region 2 as shown in panel **B** represents the fluorescence ratio in the Y axis. Line
918 shows linear regression fit with R^2 value = 0.308 and p= 1.72 x 10^{-5}. (n=5-7 root hairs
919 per time point).
920
921 **Figure 2.** SPI-YPet is Localized to Brefeldin A (BFA) Sensitive Post-Golgi
922 Compartments.
923 **(A)** Brightfield and corresponding fluorescence image of an elongating root hair showing
924 the accumulation of SPI-YPet at the apical dome in solvent control-treated seedlings.
925 **(B)** Brightfield and corresponding fluorescence image of an elongating root hair 10 min
926 after treatment with 50 μM BFA. SPI-YPet at the root hair tip dissipates and forms
927 fluorescent agglomerates along the subapical regions (arrows).
928 **(C)** SPI-YPet signal is undetectable in the elongation zone of solvent control-treated
929 roots. Within 10 min of BFA application, distinct SPI-YPet fluorescent agglomerates

930 (arrows) form. Representative low (middle panel) and high (right panel) magnification
931 images of the elongation zone of BFA-treated roots are shown.
932 **(D)** and **(E)** The bulk secretory marker, SEC-RFP, accumulates at the tips of growing
933 wild-type root hairs (arrowhead), but is absent in *spi* root hairs (**).
934 **(F)** Box plot of SEC-RFP root hair tip accumulation expressed as fluorescence ratio.
935 Ratio values were obtained by dividing mean fluorescence in oval region in 1 over
936 region 2 (inset). Box limits indicate 25th percentile and 75th percentile, horizontal line is
937 the mean and whiskers display min and max values. Asterisk (***) indicates statistical
938 significance (p<0.001) as determined by Student's T-test. Bars = 10 μm (**A**, **B** and **D**);
939 bars in **(C)** = 50 μm. Means (n = 8-10 root hairs) ± SE
940
941 **Figure 3.** The Tip-focused F-actin Meshwork is Disrupted in Root Hairs of *spi*.
942 **(A)** to **(D)** Time course of F- actin organization in a wild-type root hair from bulge
943 formation to rapid tip growth. Weakly fluorescing F-actin networks (**) in the root hair
944 bulge **(A)** reorganize into prominent tip-focused meshworks as the root hair transitions
945 to rapid tip growth (arrows in **B** to **D**).
946 **(E)** Tip-focused F-actin meshworks (arrow) remain prominent in a long, rapidly
947 elongating wild-type root hair.
948 **(F)** Tip-focused F-actin meshworks in wild-type root hairs are replaced with F-actin
949 bundles (arrowheads) that protrude to the tip when growth stops.
950 **(G)** to **(J)** Time course of F- actin organization in a *spi* root hair bulge that is unable to
951 transition to tip growth. Distinct F-actin meshworks are unable to form in root hair bulges
952 that terminate tip growth (**, **I**). Thick F-actin bundles eventually form in these short,
953 non-growing root hair bulges (arrowhead, **J**).
954 **(K)** to **(N)** F-actin organization in slow-growing *spi* root hairs. Some *spi* root hairs show
955 the tip-focused F-actin meshworks typically observed in wild type (arrow, **K, L**).
956 However, tip-focused F-actin meshworks in slow-growing *spi* root hairs either dissipate
957 (**, **M**) or prematurely form thick F-actin bundles that protrude to the tip (arrow, **N**).
958 **(O)** Representative maximum projection images and corresponding computer-
959 generated cross-sections of wild-type and *spi* root hair tips. The fluorescence ratio of

960 the root hair tip (oval in 1) to background (oval in 2) was used to quantify tip-focused F-
961 actin meshworks.
962 **(P)** Box plot showing tip-focused F-actin fluorescence ratio. Box limits indicate 25th
963 percentile and 75th percentile, horizontal line is the mean and whiskers display min and
964 max values. Asterisk (***) indicates statistical significance (p<0.001) as determined by
965 Student's T-test. Means (n = 18-21 root hairs) ± S.E.
966 **(Q)** Elongating root hair simultaneously expressing SPI-YPet and mRuby-Lifeact. Note
967 that SPI-positive post-Golgi compartments and F-actin meshworks colocalize at the root
968 hair apex (arrows). Bars = 10 μm.
969
970 **Figure 4.** BRK1 and SCAR2 Mark the Root Hair Initiation Domain and Contribute to
971 Planar Polarity.
972 **(A)** Maximum projection confocal micrograph of the elongation and maturation zone of
973 an *Arabidopsis* primary root expressing a functional BRK1-YFP fusion. The image was
974 generated by merging 50 Z sections taken at 0.5 μm intervals. BRK1-YFP accumulates
975 in the basal end walls and root hair initiation domains (arrows). Bar = 50 μm.
976 **(B)** Time course of BRK1-YFP depletion in a developing root hair. BRK1-YFP signal
977 (arrows) is strongest prior to the formation of a root hair bulge (0 min) and gradually
978 dissipates as the root hair undergoes rapid tip growth (35-50 min **). Bar = 20 μm.
979 **(C)** A scatter plot showing an inverse relationship between BRK1-YFP signal and root
980 hair growth rate. Ratio of fluorescence of BRK1-YFP (a) to background (b) (inset) was
981 plotted against root hair growth rate. Line shows linear regression fit with R^2 value =
982 0.2667 and p= 1.131 x 10^{-7}. (n=5-7 root hairs per time point).
983 **(D)** Time course of SCAR2-mCherry in a developing root hair. Like BRK1-YFP, SCAR2-
984 mCherry signal is strongest at the RHID and early stages of root hair bulge formation (0
985 min). SCAR2-mCherry signal dissipates when the root hair undergoes rapid tip growth
986 (40 min **). Bar = 20 μm.
987 **(E)** Brightfield microscopy images of representative trichoblasts from 6-d-old seedlings
988 showing apical shift in root hair position of *brk1* compared to wild type, and
989 complementation of *brk1* planar polarity phenotypes by BRK1-YFP. Arrowheads mark

990 the end walls of the trichoblast and asterisks (***) mark the basal wall of the emerged
991 root hair.
992 **(F)** Violin plot of root hair planar polarity in wild type, *brk1, scar1234, BRK1-YFP in brk1*
993 and *SCAR2-mCherry* in *scar1234* genotypes. Relative root hair position was obtained
994 by taking the ratio of the distance from the basal trichoblast wall (bottom arrows in **E**) to
995 the basal root hair wall (***) over the total length of the trichoblasts (i.e. length between
996 the two arrows). The plot illustrates kernel probability density in which the width
997 represents distribution of data points. The black dot is the mean and whiskers display
998 min and max values. Statistical significance was determined using non-parametric, two
999 sample Kolmogorov-Smirnov (KS) test. Wild type versus *brk1* (***$p < 2.2 \times 10^{-16}$); *brk1*
1000 versus BRK1-YFP in *brk1* (***$p=6.812 \times 10^{-18}$); Wild type versus BRK1-YFP (p=0.202
1001 not significant, *ns*); Wild type versus *scar1234* (***$p < 2.2 \times 10^{-16}$); *brk1* versus *scar1234*
1002 (p= 0.699, *ns*); *scar1234* versus SCAR2-mCherry in *scar1234* (***$p < 2.2 \times 10^{-16}$); Wild
1003 type versus *SCAR2-mCherry* in *scar1234* (*p=0.012). n = 90-117 root hairs ±S.E.
1004
1005 **Figure 5.** Depletion of BRK1 as Root Hairs Transition to Tip Growth is Delayed in *spi*
1006 **(A)** Dual imaging of BRK1-mRuby3 (arrow) and SPI-YPet shows that dissipation of
1007 BRK1 (**) coincides with accumulation of SPI (arrow) as root hairs transition to rapid tip
1008 growth.
1009 **(B)** and **(C)** BRK1-YFP signal persists in *spi* root hair bulges (arrows in **B**) that fail to
1010 transition to tip growth and in slow-growing *spi* root hairs (arrows in **C**). Bars = 20 μm.
1011 **(D)** Accumulation of SPI-YPet at the root hair tip is not altered in *brk1*. Bar = 20 μm
1012
1013 **Figure 6.** *SPI* Genetically Interacts with *BRK1* during Root Hair Development.
1014 **(A)** Representative root hair images of wild type, *brk1*, *spi* and *spi brk1*. Note that *brk1*
1015 exhibits wild type-like root hair morphology while *spi brk1* is more similar to *spi.* Bar =
1016 200 μm
1017 **(B)** and **(C)** Violin plots of root hair length **(B)** and root hair planar polarity **(C)** in wild
1018 type, *brk1, spi* and *spi brk1* genotypes. The plots illustrate kernel probability density in
1019 which the width represents proportion of data points. The black dot is the mean and
1020 whiskers display min and max values. Statistical significance was determined using

1021 non-parametric, two sample Kolmogorov-Smirnov (KS) test. For data in **(B)** wild type
1022 versus *brk1* (**p*= 0.00894); wild type versus *spi* (****p*<2.2 x 10^{-16}); wild type versus *spi*
1023 *brk1* (****p*<2.2 x 10^{-16}); *brk1* versus *spi* (****p*<2.2 x 10^{-16}); *brk1* versus *spi brk1*
1024 (****p*<2.2 x 10^{-16}); *spi* versus *spi brk1* (p=0.2145, not significant, *ns*). For data in **(C)** wild
1025 type versus *brk1* (****p*= 9.703 x 10^{-11}); wild type versus *spi* (****p*<2.2 x 10^{-16}); wild type
1026 versus *spi brk1* (****p*=6.661 x 10^{-16}); *brk1* versus *spi* (****p*=1.564 x 10^{-7}); *brk1* versus
1027 *spi brk1* (****p*=1.32 x 10^{-6}); *spi* versus *spi brk1* (p=0.9774, not significant, *ns*). Means (n
1028 = 83-110 root hairs) ± S.E.
1029
1030 **Figure 7.** *SPI* and *ARP2/3* Genetically Interact during Root Hair Development
1031 **(A)** Representative root hair images of wild type, *arp3, spi* and *spi arp3*. Note that *arp3*
1032 exhibits wild type-like root hair morphology. Unlike *spi*, *spi arp3* appears morphologically
1033 hairless.
1034 **(B)** Representative high magnification root hair images of *spi* and *spi arp3*. Note that *spi*
1035 *arp3* appear morphologically hairless because of a high number of aborted root hair
1036 bulges (arrows). The position in which *spi arp3* root hair bulges emerge is closer to the
1037 basal end walls (***) when compared with *spi*. Bar = 20 μm
1038 **(C)** and **(D)** Violin plots of root hair planar polarity in wild-type and *arp* mutants. The plot
1039 illustrates kernel probability density in which the width represents distribution of data
1040 points. The black dot is the mean and whiskers display min and max values. Statistical
1041 significance was determined using non-parametric Kolmogorov-Smirnov (KS) test.
1042 Different letters are significantly different based. P values for pair wise comparisons
1043 among genotypes are presented in Supplemental Table 1.
1044
1045 **Figure 8.** Hypothetical Model Illustrating SPI- and W/SCR-ARP2/3- Modulated Root
1046 Hair Development. Based on their common location at the root hair initiation domain
1047 (RHID), ROP/RAC-GTPase and ROP-GEF3 activate the W/SCR complex. This in turn
1048 activates a pool of ARP2/3 in the RHID to ensure the correct position of root hair
1049 emergence. Genetic interaction studies point to SPI and W/SCR-ARP2/3 functioning in
1050 parallel pathways during root hair initiation and early root hair bulge formation. SPI,
1051 through a yet to be determined mechanism, is recruited to the tips of root hair

1052 outgrowths via post-Golgi vesicles. SPI enrichment at the root hair tip then negatively
1053 regulates the W/SCR-ARP2/3- actin nucleation pathway as the root bulge enlarges by
1054 displacing or degrading BRK1. The antagonistic effect of SPI on BRK1 leads to the
1055 depletion of the active pool ARP2/3. Actin-mediated rapid root hair tip growth then
1056 commences predominantly through a SPI-dependent mechanism.
1057

FIGURES –Chin et al

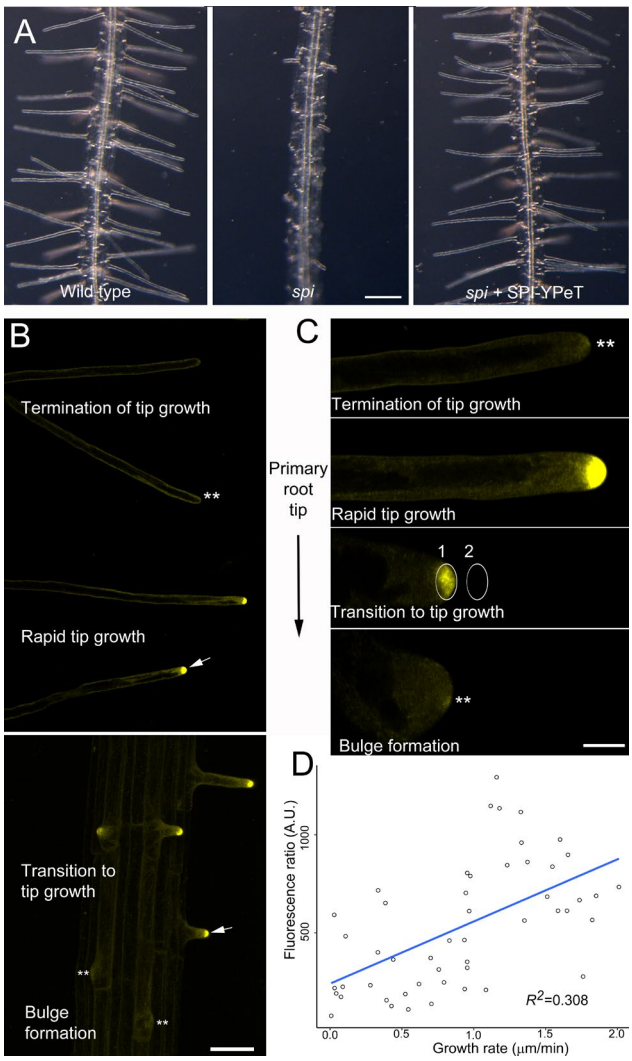

Figure 1. A Functional SPI-YPet Fusion Localizes to the Tips of Growing Root Hairs.
(A) SPI-YPet rescues the short root hair phenotype of *spi*. Bar = 100 μm.
(B) Low magnification image shows that SPI-YPet signal is most prominent at the tips of rapidly expanding root hairs (arrows). SPI-YPet signal is weak during initiation/early bulge formation and mature root hairs that have terminated tip growth (**). Bar = 50 μm
(C) High magnification images of single root hairs during bulge formation until tip growth termination. SPI-YPet is enriched at the tip of root hairs that are rapidly growing or transitioning to tip growth. Faint SPI-YPet signal is found in bulging root hairs or those that have stopped elongating (**). Bar = 10 μm.
(D) Scatter plot showing correlation analysis of root hair tip SPI-YPet fluorescence and root hair tip growth. The mean fluorescence in the oval in region 1 divided by the oval in region 2 as shown in panel **B** represents the fluorescence ratio in the Y axis. Line shows linear regression fit with R^2 value = 0.308 and p= 1.72 x 10^{-5}. (n=5-7 root hairs per time point).

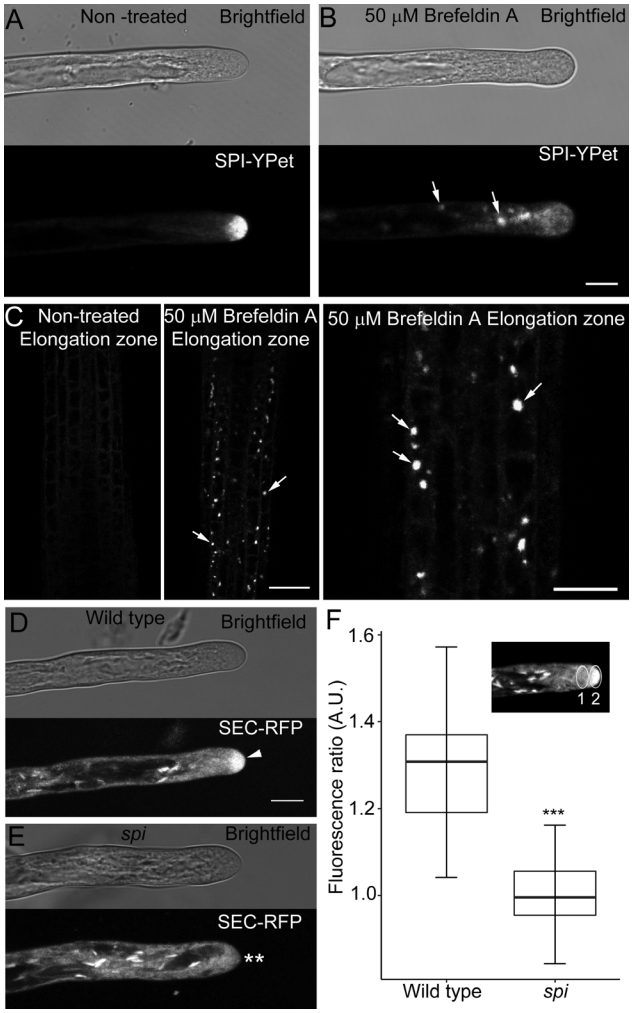

Figure 2. SPI-YPet is Localized to Brefeldin A (BFA) Sensitive Post-Golgi Compartments.

(A) Brightfield and corresponding fluorescence image of an elongating root hair showing the accumulation of SPI-YPet at the apical dome in solvent control-treated seedlings.

(B) Brightfield and corresponding fluorescence image of an elongating root hair 10 min after treatment with 50 μM BFA. SPI-YPet at the root hair tip dissipates and forms fluorescent agglomerates along the subapical regions (arrows).

(C) SPI-YPet signal is undetectable in the elongation zone of solvent control-treated roots. Within 10 min of BFA application, distinct SPI-YPet fluorescent agglomerates (arrows) form. Representative low (middle panel) and high (right panel) magnification images of the elongation zone of BFA-treated roots are shown.

(D) and **(E)** The bulk secretory marker, SEC-RFP, accumulates at the tips of growing wild-type root hairs (arrowhead), but is absent in *spi* root hairs (**).

(F) Box plot of SEC-RFP root hair tip accumulation expressed as fluorescence ratio. Ratio values were obtained by dividing mean fluorescence in oval region in 1 over region 2 (inset). Box limits indicate 25th percentile and 75th percentile, horizontal line is the mean and whiskers display min and max values. Asterisk (***) indicates statistical significance (p<0.001) as determined by Student's T-test. Bars = 10 μm (**A**, **B** and **D**); bars in **(C)** = 50 μm. Means (n = 8-10 root hairs) ± SE

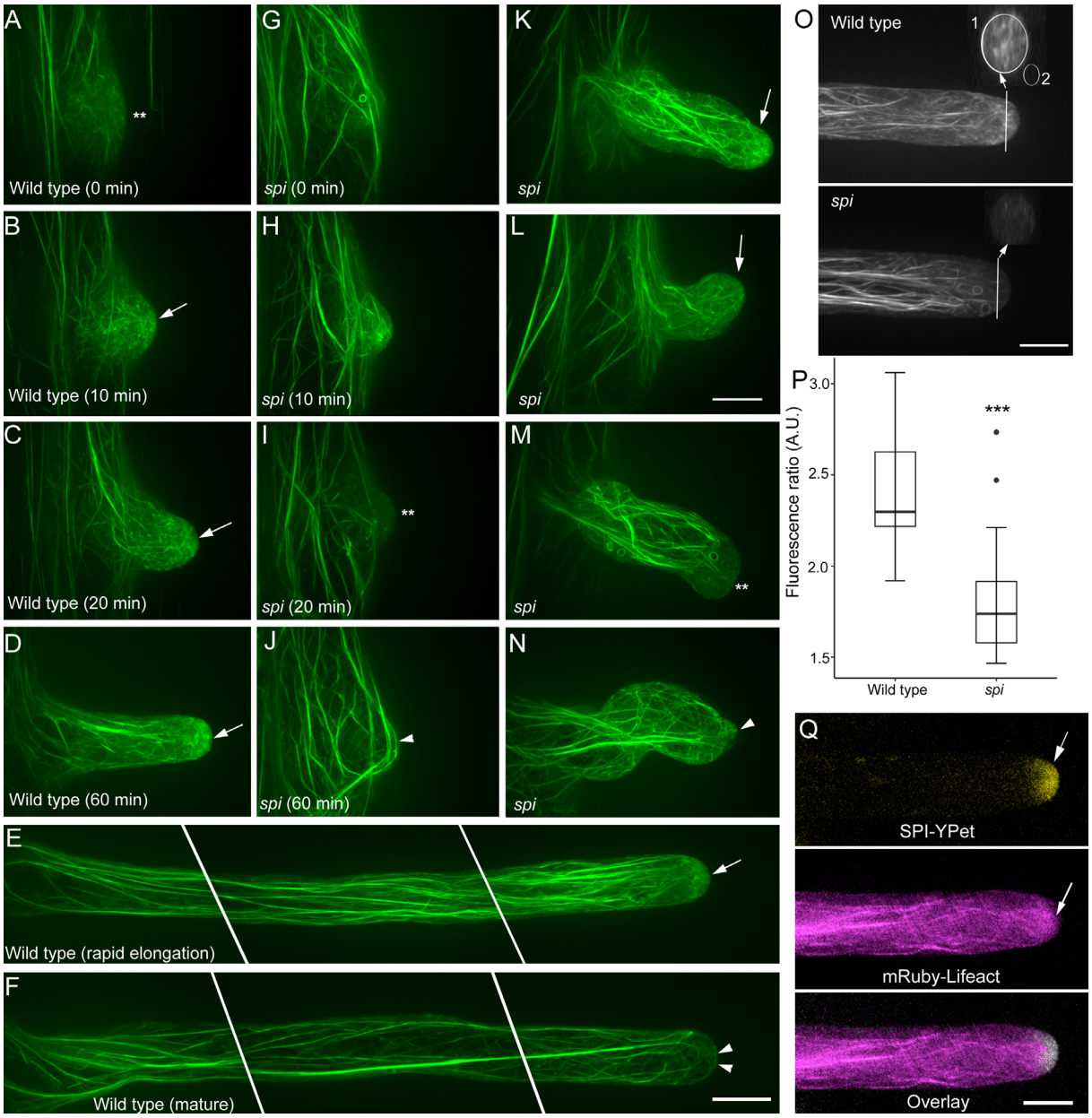

Figure 3. The Tip-focused F-actin Meshwork is Disrupted in Root Hairs of *spi*.
(A) to **(D)** Time course of F- actin organization in a wild-type root hair from bulge formation to rapid tip growth. Weakly fluorescing F-actin networks (**) in the root hair bulge **(A)** reorganize into prominent tip-focused meshworks as the root hair transitions to rapid tip growth (arrows in **B** to **D**).
(E) Tip-focused F-actin meshworks (arrow) remain prominent in a long, rapidly elongating wild-type root hair.
(F) Tip-focused F-actin meshworks in wild-type root hairs are replaced with F-actin bundles (arrowheads) that protrude to the tip when growth stops.
(G) to **(J)** Time course of F- actin organization in a *spi* root hair bulge that is unable to transition to tip growth. Distinct F-actin meshworks are unable to form in root hair bulges that terminate tip growth (**, **I**). Thick F-actin bundles eventually form in these short, non-growing root hair bulges (arrowhead, **J**).

(K) to **(N)** F-actin organization in slow-growing *spi* root hairs. Some *spi*root hairs show the tip-focused F-actin meshworks typically observed in wild type (arrow, **K, L**). However, tip-focused F-actin meshworks in slow-growing *spi* root hairs either dissipate (**, **M**) or prematurely form thick F-actin bundles that protrude to the tip (arrow, **N**).
(O) Representative maximum projection images and corresponding computer-generated cross-sections of wild-type and *spi* root hair tips. The fluorescence ratio of the root hair tip (oval in 1) to background (oval in 2) was used to quantify tip-focused F-actin meshworks.
(P) Box plot showing tip-focused F-actin fluorescence ratio. Box limits indicate 25th percentile and 75th percentile, horizontal line is the mean and whiskers display min and max values. Asterisk (***) indicates statistical significance ($p<0.001$) as determined by Student's T-test. Means (n = 18-21 root hairs) ± S.E.
(Q) Elongating root hair simultaneously expressing SPI-YPet and mRuby-Lifeact. Note that SPI-positive post-Golgi compartments and F-actin meshworks colocalize at the root hair apex (arrows). Bars = 10 μm.

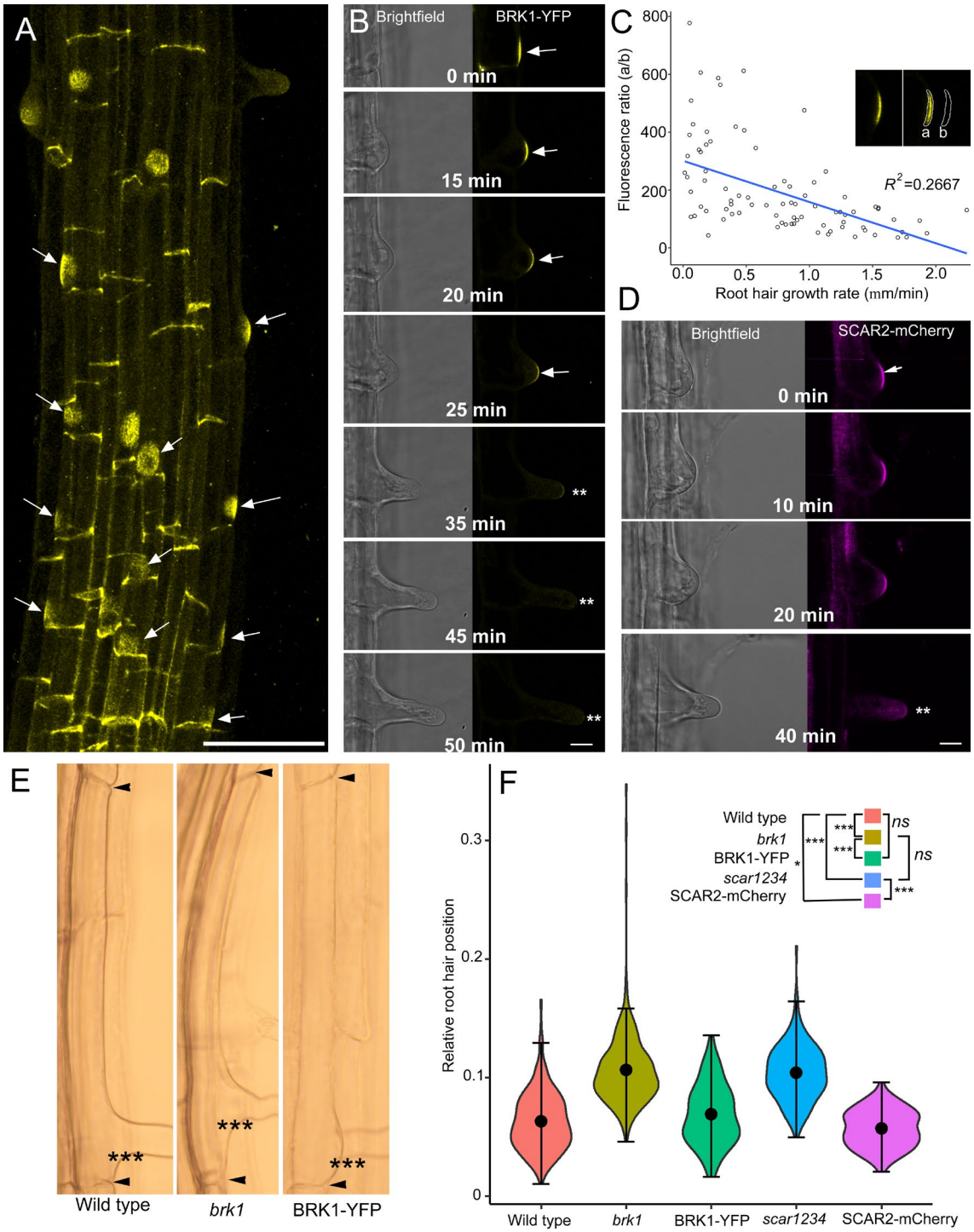

Figure 4. BRK1 and SCAR2 Mark the Root Hair Initiation Domain and Contribute to Planar Polarity.

(A) Maximum projection confocal micrograph of the elongation and maturation zone of an *Arabidopsis* primary root expressing a functional BRK1-YFP fusion. The image was generated by merging 50 Z sections taken at 0.5 μm intervals. BRK1-YFP accumulates in the basal end walls and root hair initiation domains (arrows). Bar = 50 μm.

(B) Time course of BRK1-YFP depletion in a developing root hair. BRK1-YFP signal (arrows) is strongest prior to the formation of a root hair bulge (0 min) and gradually dissipates as the root hair undergoes rapid tip growth (35-50 min **). Bar = 20 μm.
(C) A scatter plot showing an inverse relationship between BRK1-YFP signal and root hair growth rate. Ratio of fluorescence of BRK1-YFP (a) to background (b) (inset) was plotted against root hair growth rate. Line shows linear regression fit with R^2 value = 0.2667 and p= 1.131 x 10^{-7}. (n=5-7 root hairs per time point).
(D) Time course of SCAR2-mCherry in a developing root hair. Like BRK1-YFP, SCAR2-mCherry signal is strongest at the RHID and early stages of root hair bulge formation (0 min). SCAR2-mCherry signal dissipates when the root hair undergoes rapid tip growth (40 min **). Bar = 20 μm.
(E) Brightfield microscopy images of representative trichoblasts from 6-d-old seedlings showing apical shift in root hair position of *brk1* compared to wild type, and complementation of *brk1* planar polarity phenotypes by BRK1-YFP. Arrowheads mark the end walls of the trichoblast and asterisks (***) mark the basal wall of the emerged root hair.
(F) Violin plot of root hair planar polarity in wild type, *brk1, scar1234, BRK1-YFP in brk1* and *SCAR2-mCherry* in *scar1234* genotypes. Relative root hair position was obtained by taking the ratio of the distance from the basal trichoblast wall (bottom arrows in **E**) to the basal root hair wall (***) over the total length of the trichoblasts (i.e. length between the two arrows). The plot illustrates kernel probability density in which the width represents distribution of data points. The black dot is the mean and whiskers display min and max values. Statistical significance was determined using non-parametric, two sample Kolmogorov-Smirnov (KS) test. Wild type versus *brk1* (***p < 2.2 x 10^{-16}); *brk1* versus BRK1-YFP in *brk1* (***p=6.812 x 10^{-18}); Wild type versus BRK1-YFP (p=0.202 not significant, *ns*); Wild type versus *scar1234* (***p < 2.2 x 10^{-16}); *brk1* versus *scar1234* (p= 0.699, *ns*); *scar1234* versus SCAR2-mCherry in *scar1234* (***p < 2.2 x 10^{-16}); Wild type versus *SCAR2-mCherry* in *scar1234* (*p=0.012). n = 90-117 root hairs ±S.E.

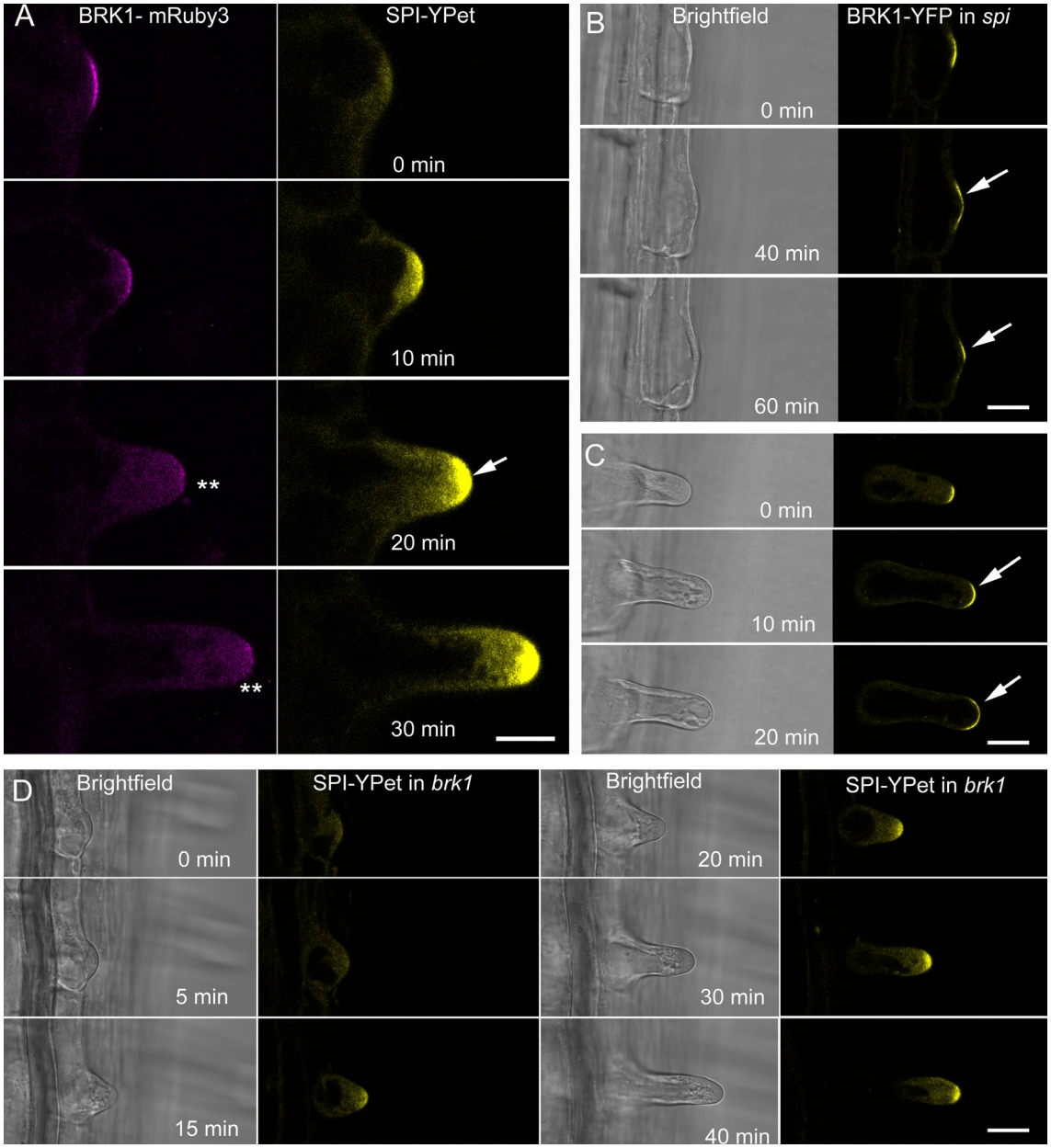

Figure 5. Depletion of BRK1 as Root Hairs Transition to Tip Growth is Delayed in *spi*
(A) Dual imaging of BRK1-mRuby3 (arrow) and SPI-YPet shows that dissipation of BRK1 (**) coincides with accumulation of SPI (arrow) as root hairs transition to rapid tip growth.
(B) and **(C)** BRK1-YFP signal persists in *spi* root hair bulges (arrows in **B**) that fail to transition to tip growth and in slow-growing *spi* root hairs (arrows in **C**). Bars = 20 μm.
(D) Accumulation of SPI-YPet at the root hair tip is not altered in *brk1*. Bar = 20 μm

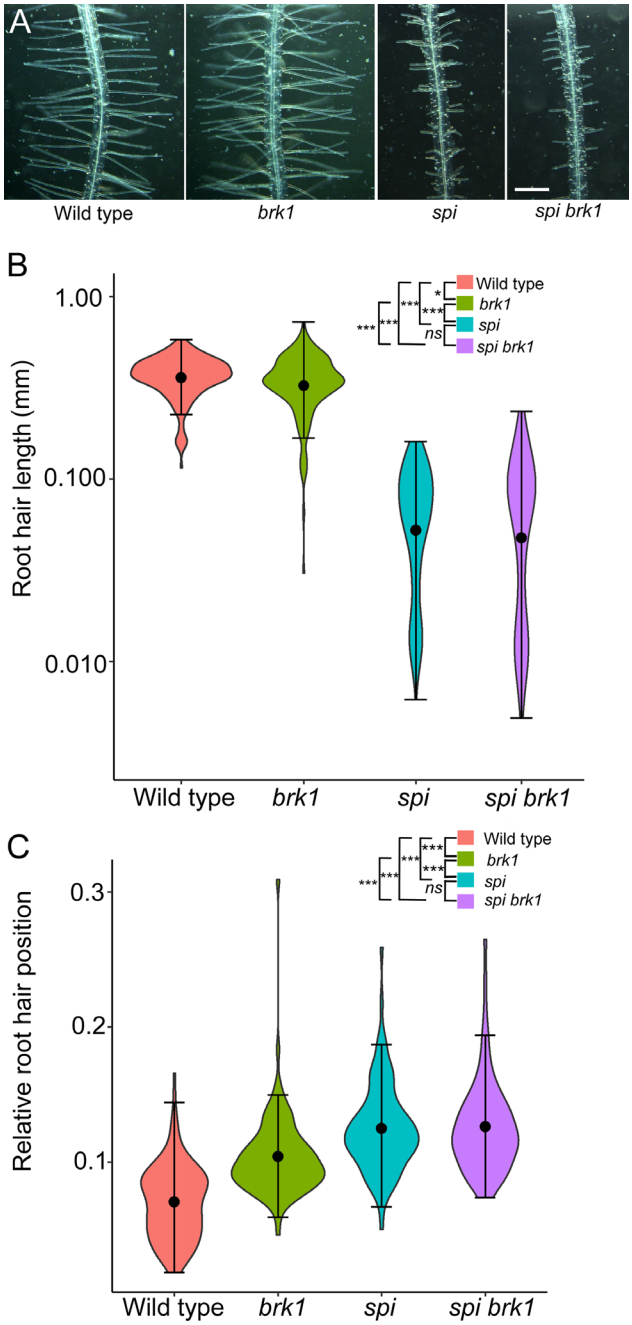

Figure 6. *SPI* Genetically Interacts with *BRK1* during Root Hair Development.
(A) Representative root hair images of wild type, *brk1*, *spi* and *spi brk1*. Note that *brk1* exhibits wild type-like root hair morphology while *spi brk1* is more similar to *spi.* Bar = 200 μm
(B) and **(C)** Violin plots of root hair length **(B)** and root hair planar polarity **(C)** in wild type, *brk1, spi* and *spi brk1* genotypes. The plots illustrate kernel probability density in which the width represents proportion of data points. The black dot is the mean and whiskers display min and max values. Statistical significance was determined using non-parametric, two sample Kolmogorov-Smirnov (KS) test. For data in **(B)** wild type versus *brk1* (**p*= 0.00894); wild type versus *spi* (****p*<2.2 x 10^{-16}); wild type versus *spi brk1* (****p*<2.2 x 10^{-16}); *brk1* versus *spi* (****p*<2.2 x 10^{-16}); *brk1* versus *spi brk1*

(***p<2.2 x 10^{-16}); *spi* versus *spi brk1* (p=0.2145, not significant, *ns*). For data in **(C)** wild type versus *brk1* (***p= 9.703 x 10^{-11}); wild type versus *spi* (***p<2.2 x 10^{-16}); wild type versus *spi brk1* (***p=6.661 x 10^{-16}); *brk1* versus *spi* (***p=1.564 x 10^{-7}); *brk1* versus *spi brk1* (***p=1.32 x 10^{-6}); *spi* versus *spi brk1* (p=0.9774, not significant, *ns*). Means (n = 83-110 root hairs) ± S.E.

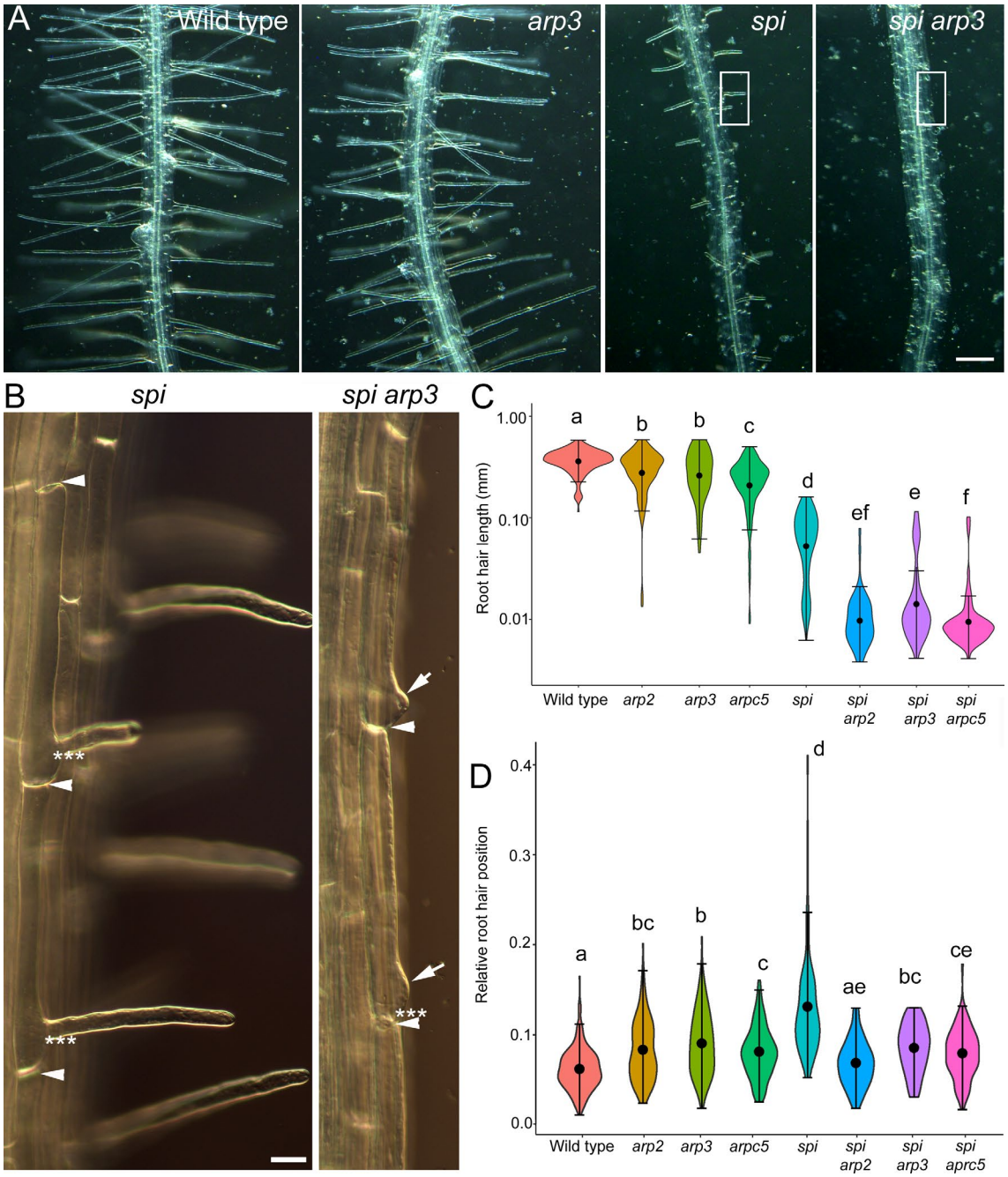

Figure 7. *SPI* and *ARP2/3* Genetically Interact during Root Hair Development

(A) Representative root hair images of wild type, *arp3, spi* and *spi arp3*. Note that *arp3* exhibits wild type-like root hair morphology. Unlike *spi*, *spi arp3* appears morphologically hairless.

(B) Representative high magnification root hair images of *spi* and *spi arp3*. Note that *spi arp3* appear morphologically hairless because of a high number of aborted root hair bulges (arrows). The position in which *spi arp3* root hair bulges emerge is closer to the basal end walls (***) when compared with *spi*. Bar = 20 μm

(C) and **(D)** Violin plots of root hair planar polarity in wild-type and *arp* mutants. The plot illustrates kernel probability density in which the width represents distribution of data

points. The black dot is the mean and whiskers display min and max values. Statistical significance was determined using non-parametric Kolmogorov-Smirnov (KS) test. Different letters are significantly different based. P values for pair wise comparisons among genotypes are presented in Supplemental Table 1.

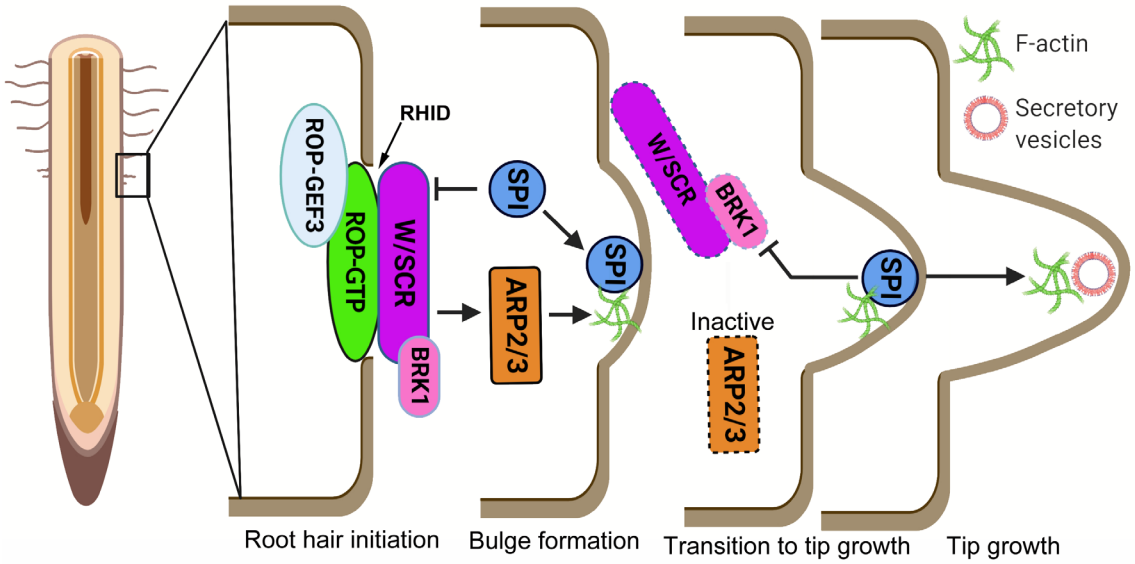

Figure 8. Hypothetical Model Illustrating SPI- and W/SCR-ARP2/3- Modulated Root Hair Development. Based on their common location at the root hair initiation domain (RHID), ROP/RAC-GTPase and ROP-GEF3 activate the W/SCR complex. This in turn activates a pool of ARP2/3 in the RHID to ensure the correct position of root hair emergence. Genetic interaction studies point to SPI and W/SCR-ARP2/3 functioning in parallel pathways during root hair initiation and early root hair bulge formation. SPI, through a yet to be determined mechanism, is recruited to the tips of root hair outgrowths via post-Golgi vesicles. SPI enrichment at the root hair tip then negatively regulates the W/SCR-ARP2/3- actin nucleation pathway as the root bulge enlarges by displacing or degrading BRK1. The antagonistic effect of SPI on BRK1 leads to the depletion of the active pool ARP2/3. Actin-mediated rapid root hair tip growth then commences predominantly through a SPI-dependent mechanism.

Parsed Citations

ALONSO, J. M., STEPANOVA, A. N., LEISSE, T. J., KIM, C. J., CHEN, H., SHINN, P., STEVENSON, D. K., ZIMMERMAN, J., BARAJAS, P., CHEUK, R., GADRINAB, C., HELLER, C., JESKE, A., KOESEMA, E., MEYERS, C. C., PARKER, H., PREDNIS, L., ANSARI, Y., CHOY, N., DEEN, H., GERALT, M., HAZARI, N., HOM, E., KARNES, M., MULHOLLAND, C., NDUBAKU, R., SCHMIDT, I., GUZMAN, P., AGUILAR-HENONIN, L., SCHMID, M., WEIGEL, D., CARTER, D. E., MARCHAND, T., RISSEEUW, E., BROGDEN, D., ZEKO, A., CROSBY, W. L., BERRY, C. C. & ECKER, J. R. 2003. Genome-Wide Insertional Mutagenesis of Arabidopsis thaliana. Science, 301, 653.
Google Scholar: Author Only Title Only Author and Title

BADET, T., LEGER, O., BARASCUD, M., VOISIN, D., SADON, P., VINCENT, R., LE RU, A., BALAGUE, C., ROBY, D. & RAFFAELE, S. 2019. Expression polymorphism at the ARPC4 locus links the actin cytoskeleton with quantitative disease resistance to Sclerotinia sclerotiorum in Arabidopsis thaliana. New Phytol, 222, 480-496.
Google Scholar: Author Only Title Only Author and Title

BALUŠKA, F. 2002. F-Actin-Dependent Endocytosis of Cell Wall Pectins in Meristematic Root Cells. Insights from Brefeldin A-Induced Compartments. Plant Physiology, 130, 422-431.
Google Scholar: Author Only Title Only Author and Title

BALUŠKA, F. 2010. Recent surprising similarities between plant cells and neurons. Plant signaling & behavior, 5, 87-89.
Google Scholar: Author Only Title Only Author and Title

BASCOM, C. S., HEPLER, P. K. & BEZANILLA, M. 2018a. Interplay between Ions, the Cytoskeleton, and Cell Wall Properties during Tip Growth. Plant Physiology, 176, 28-40.
Google Scholar: Author Only Title Only Author and Title

BASCOM, C. S., WINSHIP, L. J. & BEZANILLA, M. 2018b. Simultaneous imaging and functional studies reveal a tight correlation between calcium and actin networks. Proceedings of the National Academy of Sciences, 115, E2869-E2878.
Google Scholar: Author Only Title Only Author and Title

BASU, D., EL-ASSAL SEL, D., LE, J., MALLERY, E. L. & SZYMANSKI, D. B. 2004. Interchangeable functions of Arabidopsis PIROGI and the human WAVE complex subunit SRA1 during leaf epidermal development. Development, 131, 4345-55.
Google Scholar: Author Only Title Only Author and Title

BASU, D., LE, J., EL-ESSAL SEL, D., HUANG, S., ZHANG, C., MALLERY, E. L., KOLIANTZ, G., STAIGER, C. J. & SZYMANSKI, D. B. 2005. DISTORTED3/SCAR2 is a putative arabidopsis WAVE complex subunit that activates the Arp2/3 complex and is required for epidermal morphogenesis. Plant Cell, 17, 502-24.
Google Scholar: Author Only Title Only Author and Title

BASU, D., LE, J., ZAKHAROVA, T., MALLERY, E. L. & SZYMANSKI, D. B. 2008. A SPIKE1 signaling complex controls actin-dependent cell morphogenesis through the heteromeric WAVE and ARP2/3 complexes. Proceedings of the National Academy of Sciences, 105, 4044-4049.
Google Scholar: Author Only Title Only Author and Title

BATES, D., MAECHLER, M., BOLKER, B. & WALKER, S. 2015. Fitting Linear Mixed-Effects Models using lme4. Journal of Statistical Software, 67, 1-48.
Google Scholar: Author Only Title Only Author and Title

BIBIKOVA, T. N., BLANCAFLOR, E. B. & GILROY, S. 1999. Microtubules regulate tip growth and orientation in root hairs of Arabidopsis thaliana. The Plant Journal, 17, 657-665.
Google Scholar: Author Only Title Only Author and Title

BLANCHOIN, L., AMANN, K. J., HIGGS, H. N., MARCHAND, J.-B., KAISER, D. A. & POLLARD, T. D. 2000. Direct observation of dendritic actin filament networks nucleated by Arp2/3 complex and WASP/Scar proteins. Nature, 404, 1007-1011.
Google Scholar: Author Only Title Only Author and Title

BRUMOS, J., ZHAO, C., GONG, Y., SORIANO, D., PATEL, A. P., PEREZ-AMADOR, M. A., STEPANOVA, A. N. & ALONSO, J. M. 2020. An Improved Recombineering Toolset for Plants. The Plant Cell, 32, 100-122.
Google Scholar: Author Only Title Only Author and Title

CARMINATI, A., PASSIOURA, J. B., ZAREBANADKOUKI, M., AHMED, M. A., RYAN, P. R., WATT, M. & DELHAIZE, E. 2017. Root hairs enable high transpiration rates in drying soils. New Phytol, 216, 771-781.
Google Scholar: Author Only Title Only Author and Title

CINGOLANI, L. A. & GODA, Y. 2008. Actin in action: the interplay between the actin cytoskeleton and synaptic efficacy. Nature Reviews Neuroscience, 9, 344-356.
Google Scholar: Author Only Title Only Author and Title

CLOUGH, S. J. & BENT, A. F. 1998. Floral dip: a simplified method for Agrobacterium-mediated transformation of Arabidopsis thaliana. The Plant Journal, 16, 735-743.
Google Scholar: Author Only Title Only Author and Title

CULLINANE, A. R., SCHAFFER, A. A. & HUIZING, M. 2013. The BEACH is hot: a LYST of emerging roles for BEACH-domain containing

proteins in human disease. Traffic, 14, 749-66.
Google Scholar: Author Only Title Only Author and Title

DE MENDIBURU, F. 2020. agricolae: Statistical Procedures for Agricultural Rsearch.

DE SOUZA, N., VALLIER, L. G., FARES, H. & GREENWALD, I. 2007. SEL-2, the C. elegans neurobeachin/LRBA homolog, is a negative regulator of lin-12/Notch activity and affects endosomal traffic in polarized epithelial cells. Development, 134, 691-702.
Google Scholar: Author Only Title Only Author and Title

DEEKS, M. J. & HUSSEY, P. J. 2005. Arp2/3 and SCAR: plants move to the fore. Nat Rev Mol Cell Biol, 6, 954-64.
Google Scholar: Author Only Title Only Author and Title

DEEKS, M. J., KALORITI, D., DAVIES, B., MALHO, R. & HUSSEY, P. J. 2004. Arabidopsis NAP1 is essential for Arp2/3-dependent trichome morphogenesis. Curr Biol, 14, 1410-4.
Google Scholar: Author Only Title Only Author and Title

DENNINGER, P., REICHELT, A., SCHMIDT, V. A. F., MEHLHORN, D. G., ASSECK, L. Y., STANLEY, C. E., KEINATH, N. F., EVERS, J.-F., GREFEN, C. & GROSSMANN, G. 2019. Distinct RopGEFs Successively Drive Polarization and Outgrowth of Root Hairs. Current Biology, 29, 1854-1865.
Google Scholar: Author Only Title Only Author and Title

DJAKOVIC, S. 2006. BRICK1/HSPC300 functions with SCAR and the ARP2/3 complex to regulate epidermal cell shape in Arabidopsis. Development, 133, 1091-1100.
Google Scholar: Author Only Title Only Author and Title

DOYLE, S. M., VAIN, T. & ROBERT, S. 2015. Small molecules unravel complex interplay between auxin biology and endomembrane trafficking. Journal of Experimental Biology, 66, 4971-4982.
Google Scholar: Author Only Title Only Author and Title

DYACHOK, J., PAEZ-GARCIA, A., YOO, C. M., PALANICHELVAM, K. & BLANCAFLOR, E. B. 2016. Fluorescence Imaging of the Cytoskeleton in Plant Roots. In: GAVIN, R. H. (ed.) Cytoskeleton Methods and Protocols: Methods in Molecular Biology series. 3rd ed. Totowa, New Jersey: Humana Press.
Google Scholar: Author Only Title Only Author and Title

DYACHOK, J., SHAO, M.-R., VAUGHN, K., BOWLING, A., FACETTE, M., DJAKOVIC, S., CLARK, L. & SMITH, L. 2008. Plasma Membrane-Associated SCAR Complex Subunits Promote Cortical F-Actin Accumulation and Normal Growth Characteristics in Arabidopsis Roots. Molecular Plant, 1, 990-1006.
Google Scholar: Author Only Title Only Author and Title

DYACHOK, J., ZHU, L., LIAO, F., HE, J., HUQ, E. & BLANCAFLOR, E. B. 2011. SCAR Mediates Light-Induced Root Elongation in Arabidopsis through Photoreceptors and Proteasomes. The Plant Cell, 23, 3610-3626.
Google Scholar: Author Only Title Only Author and Title

EDWARDS, K., JOHNSTONE, C. & THOMPSON, C. 1991. A simple and rapid method for the preparation of plant genomic DNA for PCR analysis. Nucleic acids research, 19, 1349-1349.
Google Scholar: Author Only Title Only Author and Title

EL-ASSAL SEL, D., LE, J., BASU, D., MALLERY, E. L. & SZYMANSKI, D. B. 2004. Arabidopsis GNARLED encodes a NAP125 homolog that positively regulates ARP2/3. Curr Biol, 14, 1405-9.
Google Scholar: Author Only Title Only Author and Title

FASO, C., CHEN, Y. N., TAMURA, K., HELD, M., ZEMELIS, S., MARTI, L., SARAVANAN, R., HUMMEL, E., KUNG, L., MILLER, E., HAWES, C. & BRANDIZZI, F. 2009. A Missense Mutation in the Arabidopsis COPII Coat Protein Sec24A Induces the Formation of Clusters of the Endoplasmic Reticulum and Golgi Apparatus. The Plant Cell, 21, 3655-3671.
Google Scholar: Author Only Title Only Author and Title

FINKA, A., SAIDI, Y., GOLOUBINOFF, P., NEUHAUS, J. M., ZRYD, J. P. & SCHAEFER, D. G. 2008. The knock-out of ARP3a gene affects F-actin cytoskeleton organization altering cellular tip growth, morphology and development in moss Physcomitrella patens. Cell Motil Cytoskeleton, 65, 769-84.
Google Scholar: Author Only Title Only Author and Title

FISCHER, U., IKEDA, Y., LJUNG, K., SERRALBO, O., SINGH, M., HEIDSTRA, R., PALME, K., SCHERES, B. & GREBE, M. 2006. Vectorial Information for Arabidopsis Planar Polarity Is Mediated by Combined AUX1, EIN2, and GNOM Activity. Current Biology, 16, 2143-2149.
Google Scholar: Author Only Title Only Author and Title

FOX, J. & WEISBERG, S. 2019. An {R} Companion to Applied Regression, Third Edition. Thousand Oaks, CA: Sage.
Google Scholar: Author Only Title Only Author and Title

FRANK, M. J. & SMITH, L. G. 2002. A Small, Novel Protein Highly Conserved in Plants and Animals Promotes the Polarized Growth and Division of Maize Leaf Epidermal Cells. Current Biology, 12, 849-853.
Google Scholar: Author Only Title Only Author and Title

GIBBON, B. C., KOVAR, D. R. & STAIGER, C. J. 1999. Latrunculin B Has Different Effects on Pollen Germination and Tube Growth. The Plant Cell, 11, 2349-2364.

Google Scholar: Author Only Title Only Author and Title

GRIERSON, C., NIELSEN, E., KETELAAR, T. & SCHIEFELBEIN, J. 2014. Root Hairs. The Arabidopsis Book, 12.
Google Scholar: Author Only Title Only Author and Title

HARRIES, P. A., PAN, A. & QUATRANO, R. S. 2005. Actin-related protein2/3 complex component ARPC1 is required for proper cell morphogenesis and polarized cell growth in Physcomitrella patens. Plant Cell, 17, 2327-39.
Google Scholar: Author Only Title Only Author and Title

HAUBERT, D., GHARIB, N., RIVERO, F., WIEGMANN, K., HÖSEL, M., KRÖNKE, M. & KASHKAR, H. 2007. PtdIns(4,5)P-restricted plasma membrane localization of FAN is involved in TNF-induced actin reorganization. The EMBO journal, 26, 3308-3321.
Google Scholar: Author Only Title Only Author and Title

HONKANEN, S., JONES, V. A. S., MORIERI, G., CHAMPION, C., HETHERINGTON, A. J., KELLY, S., PROUST, H., SAINT-MARCOUX, D., PRESCOTT, H. & DOLAN, L. 2016. The Mechanism Forming the Cell Surface of Tip-Growing Rooting Cells Is Conserved among Land Plants. Current Biology, 26, 3238-3244.
Google Scholar: Author Only Title Only Author and Title

HÜLSKAMP, M., MISÉRA, S. & JÜRGENS, G. 1994. Genetic dissection of trichome cell development in Arabidopsis. Cell, 76, 555-566.
Google Scholar: Author Only Title Only Author and Title

ISNER, J. C., XU, Z., COSTA, J. M., MONNET, F., BATSTONE, T., OU, X., DEEKS, M. J., GENTY, B., JIANG, K. & HETHERINGTON, A. M. 2017. Actin filament reorganisation controlled by the SCAR/WAVE complex mediates stomatal response to darkness. New Phytol, 215, 1059-1067.
Google Scholar: Author Only Title Only Author and Title

JONES, M. A., SHEN, J.-J., FU, Y., LI, H., YANG, Z. & GRIERSON, C. S. 2002. The Arabidopsis Rop2 GTPase Is a Positive Regulator of Both Root Hair Initiation and Tip Growth. The Plant Cell, 14, 763-776.
Google Scholar: Author Only Title Only Author and Title

JÖRGENS, C. I., GRÜNEWALD, N., HÜLSKAMP, M. & UHRIG, J. F. 2010. A role for ABIL3 in plant cell morphogenesis. The Plant Journal, 62, 925-935.
Google Scholar: Author Only Title Only Author and Title

KIEFER, C. S., CLAES, A. R., NZAYISENGA, J. C., PIETRA, S., STANISLAS, T., HUSER, A., IKEDA, Y. & GREBE, M. 2015. Arabidopsis AIP1-2 restricted by WER-mediated patterning modulates planar polarity. Development, 142, 151-161.
Google Scholar: Author Only Title Only Author and Title

KOTCHONI, S. O., ZAKHAROVA, T., MALLERY, E. L., LE, J., EL-ASSAL, S. E.-D. & SZYMANSKI, D. B. 2009. The Association of the Arabidopsis Actin-Related Protein2/3 Complex with Cell Membranes Is Linked to Its Assembly Status But Not Its Activation. Plant Physiology, 151, 2095-2109.
Google Scholar: Author Only Title Only Author and Title

LE, J., EL-ASSAL SEL, D., BASU, D., SAAD, M. E. & SZYMANSKI, D. B. 2003. Requirements for Arabidopsis ATARP2 and ATARP3 during epidermal development. Curr Biol, 13, 1341-7.
Google Scholar: Author Only Title Only Author and Title

LE, J., MALLERY, E. L., ZHANG, C., BRANKLE, S. & SZYMANSKI, D. B. 2006. Arabidopsis BRICK1/HSPC300 Is an Essential WAVE-Complex Subunit that Selectively Stabilizes the Arp2/3 Activator SCAR2. Current Biology, 16, 895-901.
Google Scholar: Author Only Title Only Author and Title

LI, J., BLANCHOIN, L. & STAIGER, C. J. 2015. Signaling to actin stochastic dynamics. Annu Rev Plant Biol, 66, 415-40.
Google Scholar: Author Only Title Only Author and Title

LI, S., BLANCHOIN, L., YANG, Z. & LORD, E. M. 2003. The putative Arabidopsis arp2/3 complex controls leaf cell morphogenesis. Plant Physiol, 132, 2034-44.
Google Scholar: Author Only Title Only Author and Title

LI, X., LI, J. H., WANG, W., CHEN, N. Z., MA, T. S., XI, Y. N., ZHANG, X. L., LIN, H. F., BAI, Y., HUANG, S. J. & CHEN, Y. L. 2014. ARP2/3 complex-mediated actin dynamics is required for hydrogen peroxide-induced stomatal closure in Arabidopsis. Plant Cell Environ, 37, 1548-60.
Google Scholar: Author Only Title Only Author and Title

LIU, X., LI, Y., WANG, X., XING, R., LIU, K., GAN, Q., TANG, C., GAO, Z., JIAN, Y., LUO, S., GUO, W. & YANG, C. 2017. The BEACH-containing protein WDR81 coordinates p62 and LC3C to promote aggrephagy. Journal of Cell Biology, 216, 1301-1320.
Google Scholar: Author Only Title Only Author and Title

LUKOWITZ, W., GILLMOR, C. S. & SCHEIBLE, W.-R. 2000. Positional Cloning in Arabidopsis. Why It Feels Good to Have a Genome Initiative Working for You. Plant Physiology, 123, 795-806.
Google Scholar: Author Only Title Only Author and Title

MACHESKY, L. M., ATKINSON, S. J., AMPE, C., VANDEKERCKHOVE, J. & POLLARD, T. D. 1994. Purification of a cortical complex containing two unconventional actins from Acanthamoeba by affinity chromatography on profilin-agarose. The Journal of Cell Biology,

127, 107-115.
Google Scholar: Author Only Title Only Author and Title

MATHUR, J., MATHUR, N., KERNEBECK, B. & HÜLSKAMP, M. 2003. Mutations in actin-related proteins 2 and 3 affect cell shape development in Arabidopsis. The Plant Cell, 15, 1632-1645.
Google Scholar: Author Only Title Only Author and Title

MATTILA, P. K. & LAPPALAINEN, P. 2008. Filopodia: molecular architecture and cellular functions. Nature Reviews Molecular Cell Biology, 9, 446-454.
Google Scholar: Author Only Title Only Author and Title

MOLENDIJK, A. J., BISCHOFF, F., RAJENDRAKUMAR, C. S., FRIML, J., BRAUN, M., GILROY, S. & PALME, K. 2001. Arabidopsis thaliana Rop GTPases are localized to tips of root hairs and control polar growth. The EMBO journal, 20, 2779-2788.
Google Scholar: Author Only Title Only Author and Title

NAKAMURA, M. & GREBE, M. 2018. Outer, inner and planar polarity in the Arabidopsis root. Current Opinion in Plant Biology, 41, 46-53.
Google Scholar: Author Only Title Only Author and Title

NGUYEN, A. W. & DAUGHERTY, P. S. 2005. Evolutionary optimization of fluorescent proteins for intracellular FRET. Nature Biotechnology, 23, 355-360.
Google Scholar: Author Only Title Only Author and Title

NIESMANN, K., BREUER, D., BROCKHAUS, J., BORN, G., WOLFF, I., REISSNER, C., KILIMANN, M. W., ROHLMANN, A. & MISSLER, M. 2011. Dendritic spine formation and synaptic function require neurobeachin. Nature Communications, 2, 557.
Google Scholar: Author Only Title Only Author and Title

PAEZ-GARCIA, A., SPARKS, J.A., DE BANG, L., BLANCAFLOR, E.B. 2018. Plant actin cytoskeleton: New functions from old scaffold. In: SAHI, V., BALUŠKA, F. (ed.) Concepts in Cell Biology - History and Evolution. Springer.
Google Scholar: Author Only Title Only Author and Title

PÉREZ-PÉREZ, J. M., CANDELA, H. & MICOL, J. L. 2009. Understanding synergy in genetic interactions. Trends in Genetics, 25, 368-376.
Google Scholar: Author Only Title Only Author and Title

PERROUD, P. F. & QUATRANO, R. S. 2006. The role of ARPC4 in tip growth and alignment of the polar axis in filaments of Physcomitrella patens. Cell Motil Cytoskeleton, 63, 162-71.
Google Scholar: Author Only Title Only Author and Title

PERROUD, P. F. & QUATRANO, R. S. 2008. BRICK1 is required for apical cell growth in filaments of the moss Physcomitrella patens but not for gametophore morphology. Plant Cell, 20, 411-22.
Google Scholar: Author Only Title Only Author and Title

PRATAP SAHI, V., CIFROVA, P., GARCIA-GONZALEZ, J., KOTANNAL BABY, I., MOUILLE, G., GINEAU, E., MULLER, K., BALUSKA, F., SOUKUP, A., PETRASEK, J. & SCHWARZEROVA, K. 2018. Arabidopsis thaliana plants lacking the ARP2/3 complex show defects in cell wall assembly and auxin distribution. Ann Bot, 122, 777-789.
Google Scholar: Author Only Title Only Author and Title

PREUSS, M. L., SERNA, J., FALBEL, T. G., BEDNAREK, S. Y. & NIELSEN, E. 2004. The Arabidopsis Rab GTPase RabA4b Localizes to the Tips of Growing Root Hair Cells. The Plant Cell, 16, 1589-1603.
Google Scholar: Author Only Title Only Author and Title

RINGLI, C., BAUMBERGER, N., DIET, A., FREY, B. & KELLER, B. 2002. ACTIN2 is essential for bulge site selection and tip growth during root hair development of Arabidopsis. Plant Physiol, 129, 1464-72.
Google Scholar: Author Only Title Only Author and Title

ROBINSON, R. C., TURBEDSKY, K., KAISER, D. A., MARCHAND, J.-B., HIGGS, H. N., CHOE, S. & POLLARD, T. D. 2001. Crystal Structure of Arp2/3 Complex. Science, 294, 1679-1684.
Google Scholar: Author Only Title Only Author and Title

RODAL, A. A., SOKOLOVA, O., ROBINS, D. B., DAUGHERTY, K. M., HIPPENMEYER, S., RIEZMAN, H., GRIGORIEFF, N. & GOODE, B. L. 2005. Conformational changes in the Arp2/3 complex leading to actin nucleation. Nature Structural and Molecular Biology, 12, 26-31.
Google Scholar: Author Only Title Only Author and Title

RUIZ, S., KOEBERNICK, N., DUNCAN, S., FLETCHER, D. M., SCOTSON, C., BOGHI, A., MARIN, M., BENGOUGH, A. G., GEORGE, T. S., BROWN, L. K., HALLETT, P. D. & ROOSE, T. 2020. Significance of root hairs at the field scale - modelling root water and phosphorus uptake under different field conditions. Plant Soil, 447, 281-304.
Google Scholar: Author Only Title Only Author and Title

SAEDLER, R., JAKOBY, M., MARIN, B., GALIANA-JAIME, E. & HÜLSKAMP, M. 2009. The cell morphogenesis gene SPIRRIG in Arabidopsis encodes a WD/BEACH domain protein. The Plant Journal, 59, 612-621.
Google Scholar: Author Only Title Only Author and Title

SAEDLER, R., MATHUR, N., SRINIVAS, B. P., KERNEBECK, B., HÜLSKAMP, M. & MATHUR, J. 2004. Actin Control Over Microtubules Suggested by DISTORTED2 Encoding the Arabidopsis ARPC2 Subunit Homolog. Plant and Cell Physiology, 45, 813-822.

Google Scholar: Author Only Title Only Author and Title

SCHIEFELBEIN, J., HUANG, L. & ZHENG, X. 2014. Regulation of epidermal cell fate in Arabidopsis roots: the importance of multiple feedback loops. Front Plant Sci, 5, 47.
Google Scholar: Author Only Title Only Author and Title

SCHWAB, B., MATHUR, J., SAEDLER, R. R., SCHWARZ, H., FREY, B., SCHEIDEGGER, C. & HÜLSKAMP, M. 2003. Regulation of cell expansion by the DISTORTED genes in Arabidopsis thaliana: actin controls the spatial organization of microtubules. Molecular Genetics and Genomics, 269, 350-360.
Google Scholar: Author Only Title Only Author and Title

SHARAN, S. K., THOMASON, L. C., KUZNETSOV, S. G. & COURT, D. L. 2009. Recombineering: a homologous recombination-based method of genetic engineering. Nature Protocols, 4, 206-223.
Google Scholar: Author Only Title Only Author and Title

SHIBATA, M., BREUER, C., KAWAMURA, A., CLARK, N. M., RYMEN, B., BRAIDWOOD, L., MOROHASHI, K., BUSCH, W., BENFEY, P. N., SOZZANI, R. & SUGIMOTO, K. 2018. GTL1 and DF1 regulate root hair growth through transcriptional repression of ROOT HAIR DEFECTIVE 6-LIKE 4 in Arabidopsis. Development, 145, dev159707.
Google Scholar: Author Only Title Only Author and Title

SPARKS, J. A., KWON, T., RENNA, L., LIAO, F., BRANDIZZI, F. & BLANCAFLOR, E. B. 2016. HLB1 is a tetratricopeptide repeat domain-containing protein that operates at the intersection of the exocytic and endocytic pathways at the TGN/EE in Arabidopsis. The Plant Cell, 28, 746-769.
Google Scholar: Author Only Title Only Author and Title

STEFFENS, A., BRÄUTIGAM, A., JAKOBY, M. & HÜLSKAMP, M. 2015. The BEACH domain protein SPIRRIG is essential for Arabidopsis salt stress tolerance and functions as a regulator of transcript stabilization and localization. PLOS Biology, 13, e1002188.
Google Scholar: Author Only Title Only Author and Title

STEFFENS, A., JAKOBY, M. & HÜLSKAMP, M. 2017. Physical, functional and genetic interactions between the BEACH domain protein SPIRRIG and LIP5 and SKD1 and its role in endosomal trafficking to the vacuole in Arabidopsis. Frontiers in Plant Science, 8.
Google Scholar: Author Only Title Only Author and Title

STEPHAN, O. O. H. 2017. Actin fringes of polar cell growth. J Exp Bot, 68, 3303-3320.
Google Scholar: Author Only Title Only Author and Title

SUN, L., GE, Y., SPARKS, J. A., ROBINSON, Z. T., CHENG, X., WEN, J. & BLANCAFLOR, E. B. 2019. TDNAscan: A Software to Identify Complete and Truncated T-DNA Insertions. Frontiers in Genetics, 10, 685.
Google Scholar: Author Only Title Only Author and Title

SZYMANSKI, D. & STAIGER, C. J. 2018. The Actin Cytoskeleton: Functional Arrays for Cytoplasmic Organization and Cell Shape Control. Plant Physiology, 176, 106-118.
Google Scholar: Author Only Title Only Author and Title

SZYMANSKI, D. B. 2005. Breaking the WAVE complex: the point of Arabidopsis trichomes. Current Opinion in Plant Biology, 8, 103-112.
Google Scholar: Author Only Title Only Author and Title

TEAM, R. C. 2019. R: A language and environment for statistical computing. R Foundation For Statistical Computing. Vienna, Austria.
Google Scholar: Author Only Title Only Author and Title

UHRIG, J. F., MUTONDO, M., ZIMMERMANN, I., DEEKS, M. J., MACHESKY, L. M., THOMAS, P., UHRIG, S., RAMBKE, C., HUSSEY, P. J. & HULSKAMP, M. 2007. The role of Arabidopsis SCAR genes in ARP2-ARP3-dependent cell morphogenesis. Development, 134, 967-977.
Google Scholar: Author Only Title Only Author and Title

VIDALI, L., BURKART, G. M., AUGUSTINE, R. C., KERDAVID, E., TÜZEL, E. & BEZANILLA, M. 2010. Myosin XI Is Essential for Tip Growth in Physcomitrella patens. The Plant Cell, 22, 1868-1882.
Google Scholar: Author Only Title Only Author and Title

WANG, P., RICHARDSON, C., HAWES, C. & PATRICK 2016. Arabidopsis NAP1 Regulates the Formation of Autophagosomes. Current Biology, 26, 2060-2069.
Google Scholar: Author Only Title Only Author and Title

WANG, X., HERBERG, F. W., LAUE, M. M., WÜLLNER, C., HU, B., PETRASCH-PARWEZ, E. & KILIMANN, M. W. 2000. Neurobeachin: A Protein Kinase A-Anchoring,beige/Chediak-Higashi Protein Homolog Implicated in Neuronal Membrane Traffic. The Journal of Neuroscience, 20, 8551-8565.
Google Scholar: Author Only Title Only Author and Title

WICKHAM, H. 2016. ggplot2: Elegant Graphics for Data Analysis. Springer-Verlag New York.
Google Scholar: Author Only Title Only Author and Title

YANAGISAWA, M., ALONSO, J. M. & SZYMANSKI, D. B. 2018. Microtubule-Dependent Confinement of a Cell Signaling and Actin Polymerization Control Module Regulates Polarized Cell Growth. Current Biology, 28, 2459-2466.e4.

Google Scholar: Author Only Title Only Author and Title

YANAGISAWA, M., DESYATOVA, A. S., BELTETON, S. A., MALLERY, E. L., TURNER, J. A. & SZYMANSKI, D. B. 2015. Patterning mechanisms of cytoskeletal and cell wall systems during leaf trichome morphogenesis. Nature Plants, 1, 15014.
Google Scholar: Author Only Title Only Author and Title

YANAGISAWA, M., ZHANG, C. & SZYMANSKI, D. B. 2013. ARP2/3-dependent growth in the plant kingdom: SCARs for life. Frontiers in Plant Science, 4.
Google Scholar: Author Only Title Only Author and Title

YOO, C. M., QUAN, L., CANNON, A. E., WEN, J. & BLANCAFLOR, E. B. 2012. AGD1, a class 1 ARF-GAP, acts in common signaling pathways with phosphoinositide metabolism and the actin cytoskeleton in controlling Arabidopsis root hair polarity. Plant J, 69, 1064-76.
Google Scholar: Author Only Title Only Author and Title

ZHANG, C., MALLERY, E. L., SCHLUETER, J., HUANG, S., FAN, Y., BRANKLE, S., STAIGER, C. J. & SZYMANSKI, D. B. 2008. Arabidopsis SCARs Function Interchangeably to Meet Actin-Related Protein 2/3 Activation Thresholds during Morphogenesis. The Plant Cell, 20, 995-1011.
Google Scholar: Author Only Title Only Author and Title

ZHANG, X., DYACHOK, J., KRISHNAKUMAR, S., SMITH, L. G. & OPPENHEIMER, D. G. 2005. IRREGULAR TRICHOME BRANCH1 in Arabidopsis encodes a plant homolog of the actin-related protein2/3 complex activator Scar/WAVE that regulates actin and microtubule organization. Plant Cell, 17, 2314-26.
Google Scholar: Author Only Title Only Author and Title

ZHAO, Y., PAN, Z., ZHANG, Y., QU, X., ZHANG, Y., YANG, Y., JIANG, X., HUANG, S., YUAN, M., SCHUMAKER, K. S. & GUO, Y. 2013. The actin-related Protein2/3 complex regulates mitochondrial-associated calcium signaling during salt stress in Arabidopsis. Plant Cell, 25, 4544-59.
Google Scholar: Author Only Title Only Author and Title

ZHOU, R., BENAVENTE, L. M., STEPANOVA, A. N. & ALONSO, J. M. 2011. A recombineering-based gene tagging system for Arabidopsis. The Plant Journal, 66, 712-723.
Google Scholar: Author Only Title Only Author and Title

ZOU, J.-J., ZHENG, Z.-Y., XUE, S., LI, H.-H., WANG, Y.-R. & LE, J. 2016. The role of Arabidopsis Actin-Related Protein 3 in amyloplast sedimentation and polar auxin transport in root gravitropism. Journal of Experimental Botany, 67, 5325-5337.
Google Scholar: Author Only Title Only Author and Title